ARTICLE OPEN

Check for updates

Cognitive and synaptic impairment induced by deficiency of autism risk gene *Smarcc2* and its rescue by histone deacetylase inhibition

Pei Li[1], Siqi Men[1], Prachetas J. Patel[1], Komal Saleem[1], Ping Zhong[1], Kin Wai Tam[1], Jian Feng[1] and Zhen Yan[1]✉

SMARCC2, which encodes BAF170, a core subunit of chromatin remodeling BAF complex, is one of the top-ranking risk genes for autism spectrum disorder (ASD). However, the mechanisms linking *SMARCC2* haploinsufficiency to ASD remain poorly understood. ChIP-seq of *SMARCC2* demonstrated its binding to many other ASD risk genes involved in transcriptional regulation. SMARCC2 expression was significantly reduced in the nuclear fraction of postmortem prefrontal cortex (PFC) from patients with ASD. *Smarcc2* deficiency in PFC of adolescent mice led to impaired working memory, with largely intact social and anxiety-like behaviors. Significant downregulation of genes enriched in synaptic transmission was found in PFC of S*marcc2*-deficient mice by RNA-seq and qPCR profiling. Furthermore, *SMARCC2* was reduced in human iPSC-derived neurons (hiPSC-N) from ASD patients, and synaptic genes were downregulated by *SMARCC2* knockdown in hiPSC-N. In parallel, electrophysiological recordings uncovered the significant impairment of GABAergic and glutamatergic synaptic currents in PFC pyramidal neurons of S*marcc2*-deficient mice. Smarcc2 bound to HDAC2, and *Smarcc2* deficiency led to the reduced global histone acetylation and H3K9ac enrichment at synaptic gene promoters. Treatment of S*marcc2*-deficient mice with romidepsin, a class I HDAC inhibitor, normalized histone acetylation, working memory, synaptic genes and currents. These findings highlight the critical role of *Smarcc2* in regulating cognitive and synaptic function, suggesting that targeting HDAC could alleviate deficits in *Smarcc2*-associated neurodevelopmental disorders.

Molecular Psychiatry; https://doi.org/10.1038/s41380-026-03848-1

INTRODUCTION

Autism Spectrum Discorder (ASD) and intellectual disability (ID) are complex neurodevelopmental disorders, with 30–80% ASD cases accompanied by ID [1]. Growing evidence highlights the significant contribution of genetic factors to both ASD and ID [2–4]. Many of the top-ranking ASD risk genes function as histone modifiers and chromatin remodelers [2], suggesting the critical role of epigenetic mechanisms in ASD pathogenesis and therapeutic intervention [5–10].

SMARCC2, which encodes BAF170, a key subunit of the ATP-dependent chromatin remodeling BAF complex (mammalian SWI/SNF complex) [11, 12], is one of the top-ranking ASD risk genes [2, 13]. The SWI/SNF subfamily provides nucleosome rearrangement, enabling binding of specific transcription factors [14] and allowing genes to be activated or repressed [15]. Haploinsufficiency of *SMARCC2* causes a syndrome characterized by ID, developmental delay (DD), and ASD. In reported cohorts, 85% of individuals showed DD and/or ID (mild: 38%; moderate/severe: 47%), 34% displayed autistic behaviors, and 28% had seizures [16, 17]. Preclinical studies suggest that Smarcc2 plays a critical role in early development of forebrain [18], as well as proliferation and differentiation of neural stem cells in dentate gyrus of hippocampus [19]. Notably, constitutive *Smarcc2* knockout results in perinatal lethality, whereas cortex-specific deletion of *Smarcc2* causes an enlarged cortex because of increased neurogenesis [20], limiting the utility of developmental *Smarcc2* knockout models for investigating the postnatal neuronal functions of Smarcc2.

It remains unknown whether *SMARCC2* deficiency is linked to synaptic dysfunction underlying ASD/ID phenotypes. Thus, we used the virus-mediated approach to knock down *Smarcc2* in adolescent mice and examined the consequences at genomic, electrophysiological and behavioral levels. Prefrontal cortex (PFC), which controls cognitive & emotional processes and is highly disrupted in ASD [21–23], was selected for *Smarcc2* knockdown. In addition, we uncovered a therapeutic strategy to alleviate the abnormalities of *Smarcc2*-deficient mice.

RESULTS

SMARCC2-binding genes are enriched in ASD risk factors, and SMARCC2 is reduced in ASD

To understand how SMARCC2 is linked to ASD, we first examined the target genes of SMARCC2. Among the top 2000 genes with SMARCC2 binding at their promoters (1 kb of TSS), we found that 179 genes overlapped with SFARI ASD gene dataset (1128 genes) (1.59-fold over-enrichment, hypergeometric *p*-value: 1.64E-10,

[1]Department of Physiology and Biophysics, Jacobs School of Medicine and Biomedical Sciences, State University of New York at Buffalo, Buffalo, NY 14203, USA.
✉email: zhenyan@buffalo.edu

Received: 9 January 2026 Revised: 16 June 2026 Accepted: 20 August 2026
Published online: 26 August 2026

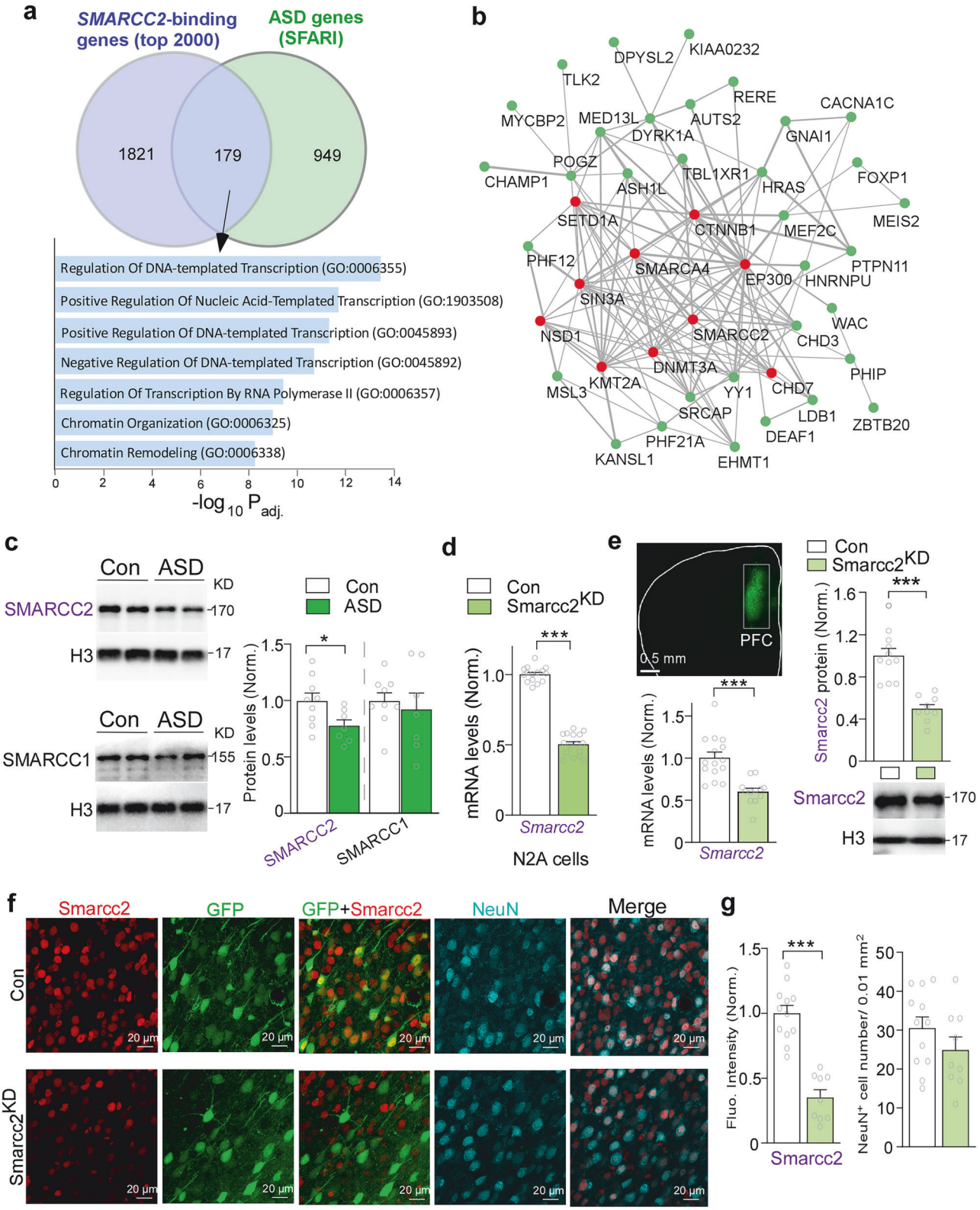

Supplementary Table 1). Gene Ontology (GO) enrichment analysis revealed that these overlapping genes had significant enrichment in pathways related to DNA-templated transcription regulation, gene expression, and chromatin remodeling (Fig. 1a). Among the 232 SFARI category I ASD genes, 43 had SMARCC2 binding at their promoters, and they formed a well-connected protein-protein interaction (PPI) network (Fig. 1b). Hub genes in the PPI network included histone acetyltransferase (*EP300*), histone methyltransferases (*SETD1A*, *KMT2A*, *NSD1*), chromatin remodelers (*SMARCA4*, *CHD7*), DNA methyltransferase (*DNMT3A*), transcriptional repressor (*SIN3A*), and dual functional gene involved in cell-cell adhesion and transcription (*CTNNB1*). These findings suggest that SMARCC2

Fig. 1 SMARCC2 binds to other ASD risk genes, and is downregulated in postmortem PFC of ASD patients. a Venn diagrams showing the significant overlap of top 2000 SMARCC2-binding genes identified from ChIP-seq data with ASD risk genes from SFARI database ($p = 1.64 \times 10^{-10}$, hypergeometric t test). Inset: Bar graphs showing the gene ontology (GO) enrichment pathways for overlapping genes. **b** Protein-protein interaction (PPI) network of SMARCC2 binding genes that belong to category 1 SFARI ASD risk genes. **c** Western blot data showing SMARCC2 and SMARCC1 levels in postmortem PFC from control and ASD patients. $n = 7$–9 human subjects/group, SMARCC2: $t_{14} = 2.3$, $p = 0.038$, t-test; SMARCC1: $t_{14} = 0.48$, $p = 0.64$, t-test. **d** Bar graphs showing *Smarcc2* mRNA levels in N2A cells transfected with control vs. *Smarcc2* shRNA. $n = 15$–16 cultures/group; $t_{29} = 20.3$, $p < 0.001$, t-test. **e** Representative low-magnification (2×) image showing the AAV injection site and bar graphs displaying *Smarcc2* mRNA and protein levels in mouse PFC injected with a control AAV vs. *Smarcc2* shRNA AAV. Inset: immunoblots of Smarcc2 and Histone H3. mRNA: $n = 12$–15 mice/group; $t_{25} = 4.78$, $p < 0.001$. Protein: $n = 9$–11 mice/group; $t_{18} = 5.9$, $p < 0.001$, t-test. Scale bars: 0.5 mm. **f** Representative confocal images (63×) showing immunostaining of Smarcc2 (red) and NeuN (blue). Scale bars: 20 μm. **g** Quantification of the fluorescence intensity of Samrcc2 and the number of NeuN+ cells. $n = 9$–12 images/3–4 mice/ group. Smarcc2 intensity: $t_{19} = 7.4$, $p < 0.001$, t-test. All data are shown as mean ± SEM, $^{*}p < 0.05$, $^{***}p < 0.001$.

could regulate gene expression and cellular function directly or indirectly through other interacting ASD genes.

To find out whether SMARCC2 expression is changed in idiopathic ASD, we examined the level of SMARCC2 protein in nuclear fraction of postmortem PFC from ASD patients. As shown in Fig. 1c, SMARCC2 protein level was significantly decreased in ASD, compared to age- and sex-matched controls, while SMARCC1 protein, which works as a scaffold protein in BAF complex like SMARCC2, did not show significant changes in ASD patients.

To find out how *SMARCC2* haploinsufficiency is linked to ASD, we performed the virus-based knockdown of *Smarcc2*. *Smarcc2* mRNA was significantly reduced in N2A cells transfected with *Smarcc2* shRNA, confirming the knockdown (KD) effectiveness (Fig. 1d). Next, *Smarcc2* shRNA AAV or a control AAV was stereotaxically injected bilaterally into the medial PFC of 5-week-old C57BL/6J mice (Fig. 1e). Two weeks post-injection, we detected the significant reduction of *Smarcc2* mRNA and protein levels in the PFC of Smarcc2^{KD} mice (Fig. 1e). A marked decrease of Smarcc2 fluorescence intensity was also observed in immunostaining, while the number of NeuN+ neurons was unchanged by *Smarcc2* knockdown (Fig. 1f and g).

Smarcc2 deficiency in mouse PFC impairs cognitive function without affecting other behaviors

Next, we assessed behavioral consequences of *Smarcc2* knockdown. Since *de novo SMARCC2* variants are associated with ID, we first evaluated cognitive function by examining working memory using spontaneous T-maze alternation tests [24] and spatial memory using Barnes Maze (BM) tests [25]. Compared to control mice, correctness in T-maze tests of Smarcc2^{KD} mice were significant decreased across trials (Fig. 2a). In BM tests, Smarcc2^{KD} mice showed no significant changes in spatial memory index (Time on correct hole / Time on all incorrect holes), while there was an increased latency to the correct hole (Fig. 2b). These results suggest that *Smarcc2* deficiency in PFC impairs cognitive function, especially working memory.

Given the strong association of *Smarcc2* haploinsufficiency to autism, we further investigated repetitive behavior and sociability, which are related to core symptoms of autism. Self-grooming, a marker of repetitive behavior, was unaffected by *Smarcc2* KD (Fig. 2c). Social behavior was assessed using three-chamber social preference tests [6, 26]. No significant alteration was found in Smarcc2^{KD} mice on social preference index and the time spent interacting with a social or non-social objects (Fig. 2d), suggesting that sociability is largely normal.

We also examined anxiety-related behaviors using elevated plus maze (EPM) tests, light-dark box (LDB) tests, and open field (OF) tests [27]. In all these measurements, compared to controls, Smarcc2^{KD} mice displayed no significant differences (Fig. 2e–g). Additionally, in resident-intruder tests, male Smarcc2^{KD} mice exhibited no change in the frequency or time of aggressive encounters or total interactions (Fig. 2h).

Smarcc2 deficiency in mouse PFC induces the downregulation of synaptic genes

Since Smarcc2 is a core subunit of BAF chromatin remodeler complex crucial for gene regulation [28], we performed RNA sequencing (RNA-seq) analysis to assess genome-wide transcriptional changes following *Smarcc2* knockdown. Using the cutoff of fold change ≥ 20% and $P_{adj.} \leq 0.05$, we identified 1735 differentially expressed genes (DEGs), with 653 downregulated and 1082 upregulated genes in Smarcc2^{KD} mice (Figure S1a, Supplementary Table 2).

GO analyses revealed that these downregulated genes were primarily enriched in synaptic transmission, transport, and signal release from synapse (Fig. 3a). Synaptic enrichment analysis with SynGO, a synaptic gene ontology database, identified presynaptic and postsynaptic genes as the most enriched components downregulated after *Smarcc2* KD (Figure S1b).

PPI of downregulated synaptic genes by *Smarcc2* knockdown (Fig. 3b) can be classified into 5 major categories, (1) glutamatergic synapse genes, including AMPA receptor (*Gria3*), NMDA receptor (*Grin2b*), glutamate transporters (*Slc1a2*, *Slc1a3*, and *Slc38a3*), (2) GABAergic synapse genes, including GABA receptors and transporters (*Gabbr1*, *Gabrb3*, *Slc6a11*, *Slc32a1*, and *Slc38a3*), GABA-synthesizing enzyme (*Gad1*), (3) synaptic vesicle release genes, including *Nrxn1*, *Syt1*, *Syn1*, *Cplx1*, *Cplx3*, and *Dnajc5*, (4) ion channels, including sodium channels (*Scn1b*, *Scn4b*, and *Scn8a*), nicotinic acetylcholine receptor (*Chrnb2*), calcium channel (*Cacng2*), potassium channel (*Kcnq3*), (5) monoamine receptors, including serotonin receptors (*Htr1b*, *Htr5a*, and *Htr3a*), and dopamine receptors (*Drd1* and *Drd2*).

Regression analysis of RNA-seq data from control vs. Smarcc2^{KD} mice revealed the strong positive correlation (Pearson r: 0.82–0.93, p: 0.013–0.00073) of the expression level of *Smarcc2* with that of synaptic genes, including *Slc32a1*, *Gad1*, *Slc1a3* (Fig. 3c), *Gria3*, *Syn1*, and *Syt1* (Figure S2).

Our analysis of the RNA-seq data of embryonic cells from *Smarcc1/2* double knockout mice [18] also found that the significantly downregulated genes were enriched in chemical synaptic transmission following nervous system development and axon guidance (Figure S3a and S3b, Supplementary Table 3). They formed a well-connected PPI network including glutamatergic synapse genes, GABAergic synapse genes, and presynaptic genes (Figure S3c), some of which overlapped with our current study (e.g. *Slc1a2/3*, *Gria3*, *Nrxn1*, *Gabrb3*, *Cplx1*).

Notably, *Smarcc2* knockdown also induced the upregulation of genes, which were enriched in extracellular matrix organization, immune response, phagocytosis, and apoptosis (Figure S4a). PPI of upregulated genes in top GO pathway pointed to key collagen genes (*Col1a1*, *Col15a1*, *Col18a1, etc.*) and matrix metalloproteinases (*Mmp14, Mmp2*) (Figure S4b).

Guided by RNA-seq data and bioinformatic analysis, we used qPCR to examine synaptic genes in larger sized samples. For GABA-related genes, a significant decrease was found in Smarcc2^{KD} mice on *Slc6a1* (encoding GAT1), *Slc32a1* (encoding

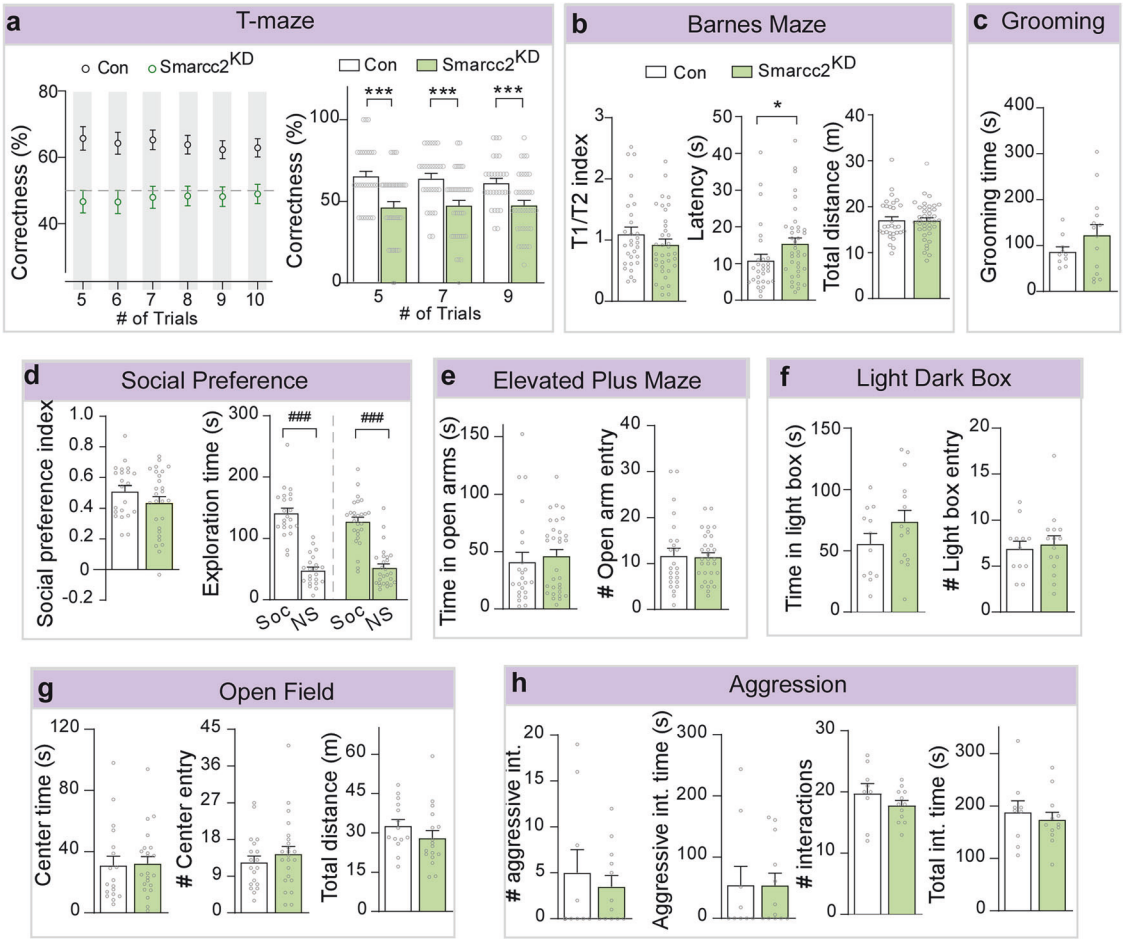

Fig. 2 ***Smarcc2*** **deficiency in PFC induces cognitive deficits without affecting other behaviors. a** Plot showing the percentage of correct responses in various trials of spontaneous T-maze tests of control vs. Smarcc2^{KD} mice. $n = 31–41$ mice/group. $p < 0.001$, t-test; (**b**) Bar graphs showing the spatial memory index and latency to the correct hole as well as total distance in Barnes Maze (BM) tests of control vs. Smarcc2^{KD} mice. $n = 29–38$ mice/group. Index: $p = 0.27$; latency: $p = 0.016$; total distance: $p = 0.73$, M-W test. **c** Bar graph showing the grooming time in grooming tests of control vs. Smarcc2^{KD} mice. $n = 10–14$ mice/group. **d** Bar graphs showing the social preference index and time spent on social (Soc) and non-social (NS) objects in three-chamber social preference tests of control vs. Smarcc2^{KD} mice. $n = 22–27$ mice/group. Time: $F_{1,94} = 147.5$, $^{###}p < 0.001$, Soc vs. NS, two-way ANOVA. **e** Bar graphs showing the time in open arms and number of entries into open arms in elevated plus maze (EPM) tests of control vs. Smarcc2^{KD} mice. $n = 24–31$ mice/group. **f** Bar graphs showing the time spent in light box and the number of entries into the light box in light-dark box tests of control vs. Smarcc2^{KD} mice. $n = 12–15$ mice/group. **g** Bar graphs showing time spent in the center area of open field, the number of entries to center area, and the total distance traveled in open field (OF) tests of control vs. Smarcc2^{KD} mice. $n = 18–22$ mice/group. **h** Bar graphs showing the number and time of aggressive encounters and total interactions in resident-intruder (RI) tests of control vs. Smarcc2^{KD} mice. $n = 9–12$ mice/group. All data are shown as mean ± SEM, $^{*}p < 0.05$, $^{***}p < 0.001$.

VGAT), and *Gad1* (Fig. 3c), while GABA receptor genes (*Gabra4*, *Gabrb2*, *Gabrg2*, *Gabrg3*), *Bsn* (encoding Bassoon), *Sst* (encoding Somatostatin), *Pvalb* (encoding Parvalbumin) and *Vip* (encoding VIP) were largely unchanged (Fig. 3c and S5a). For glutamate-related genes, a significant decrease was found in Smarcc2^{KD} mice on *Gria3* (encoding AMPAR subunit GluR3) and *Slc1a3* (encoding EAAT1), while other glutamate receptor subunits (*Gria1*, *Gria2*, *Grin1*, *Grin2a*, *Grin2b, Grm2)*, transporter or synaptic organizers (*Slc17a6*, *Homer1a*, *Nrxn1*, *Dlgap4*) were not significantly changed. Presynaptic genes for synaptic vesicle trafficking and exocytosis (*Snap25*, *Stxbp1*, *Stxbp5*, *Syp*) were also not significantly changed (Fig. 3c and Figure S5b). These data suggest that *Smarcc2* deficiency in PFC of juvenile mice induces the robust reduction of only a subset of synaptic genes.

ASD human iPSC-derived neurons (hiPSC-N) have reduced *SMARCC2* expression, and *SMARCC2* knockdown in hiPSC-N induces synaptic gene downregulation

To find out gene alterations in ASD, we generated hiPSC-derived cortical neurons from idopathic ASD patients and control subjects and performed RNA-seq to examine genome-wide changes. As shown in Fig. 4a, our hiPSC-derived cortical neurons had extensive dendritic processes and formed well-connected networks with the expression of neuronal markers MAP2 and TUJ1. RNA-seq revealed a number of differentially expressed genes (DEGs) in ASD hiPSC-derived neurons (668 downregulated, 906 upregulated, Fig. 4b, Supplementary Table 4). The downregulated genes were enriched in transcriptional regulation and chromatin organization (Fig. 4c), including many top-ranking ASD risk genes, such as *CHD8, SMARCC2, CHD2, KDM6B, ASH1L, CREBBP, POGZ*, and *FOXP1* (Fig. 4d). As shown in Fig. 4e, *SMARCC2* expression was significantly diminished in hiPSC-derived neurons from ASD patients. Regression analysis of RNA-seq data from control vs. ASD hiPSC-N also found positive correlation (Pearson r: 0.63–0.89, p: 0.093–0.0027) of the expression level of *SMARCC2* with that of synaptic genes, such as *SLC32A1*, *GRIK3, GAD1*, *GAD2*, and *PCDHB3/6* (Figure S6).

To determine the effect of *SMARCC2* deficiency on synaptic genes in human cells, we infected hiPSC-derived cortical neurons from control lines with *SMARCC2* shRNA lentivirus. As shown in Fig. 4f, mRNA levels of multiple synaptic genes were significantly

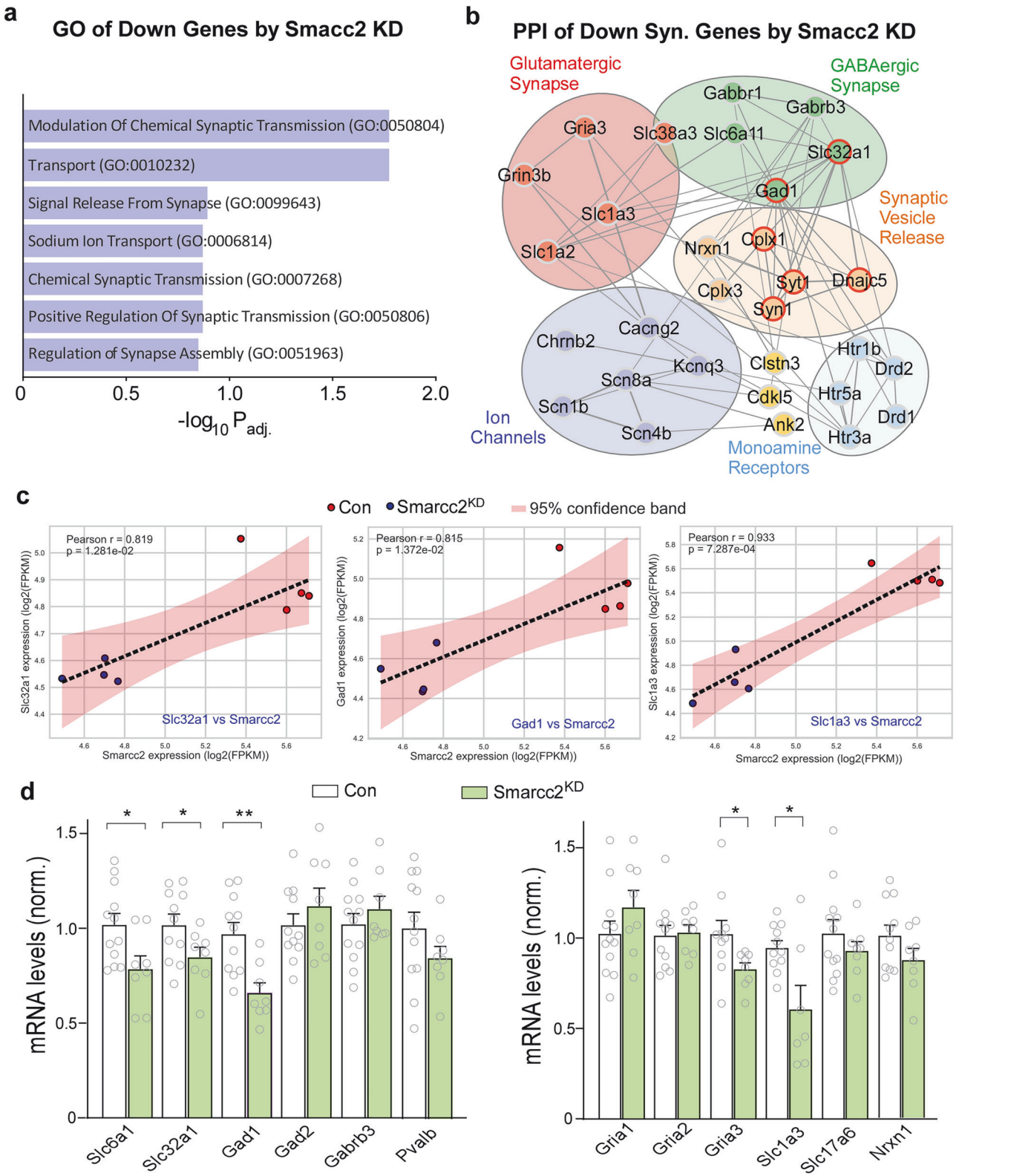

Fig. 3 RNA-seq and qPCR profiling reveals that Smarcc2 deficiency downregulates synaptic genes in PFC. a Gene Ontology (GO) enriched pathways of downregulated genes by Smarcc2 KD. **b** Protein-protein interaction (PPI) network of downregulated synaptic genes in Smarcc2^{KD} mice. Hub proteins are circled in red. **c** Correlation plots of the expression level of Smarcc2 vs. synaptic genes (*Slc32a1*, *Gad1*, *Slc1a3*) from RNA-seq data of control vs. Smarcc2^{KD} mice. $n = 4$ mice/group. **d** Bar graphs showing the mRNA level of GABAergic and glutamatergic synaptic genes in PFC of control vs. Smarcc2^{KD} mice. $n = 8$–12 mice/group. *Slc6a1*: $p = 0.02$; *Slc32a1*: $p = 0.05$; *Gad1*: $p = 0.002$; *Gria3*: $p = 0.04$; *Slc1a3*: $p = 0.009$, t-test. All data are shown as mean ± SEM, $^*p < 0.05$, $^{**}p < 0.01$.

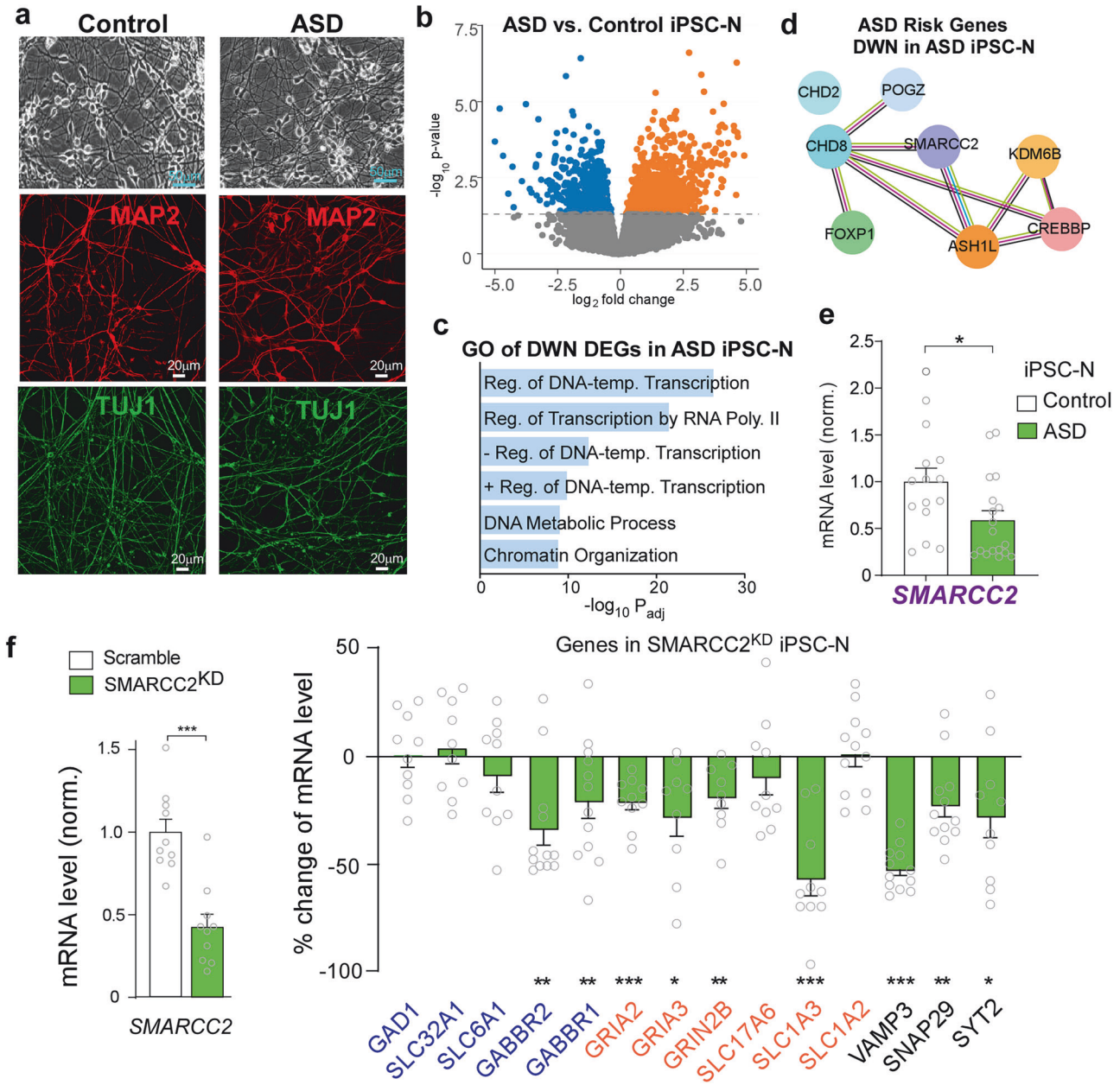

Fig. 4 ***SMARCC2* is reduced in hiPSC-N from ASD patients, and *SMARCC2* knockdown downregulates synaptic genes in hiPSC-N. a** Phase contrast and immunocytochemical images of hiPSC-derived neurons from a control and an ASD patient (Day 60) stained with neuronal markers (MAP2 and TUJ1). **b** Volcano plot showing differentially expressed genes (DEGs) in hiPSC-derived neurons from ASD vs. control subjects ($n = 4$ lines/group). **c** Gene Ontology (GO) enriched pathways of downregulated genes in hiPSC-derived neurons from ASD patients. **d** PPI network of top-ranking ASD risk genes downregulated in hiPSC-derived neurons from ASD patients. **e** Bar graphs of qPCR data showing *SMARCC2* mRNA levels in hiPSC-derived neurons from control vs. ASD patients. $n = 15$–18 cultures/4 lines/group, $U = 70$, $p = 0.02$, M-W test. $^*p < 0.05$. **f** Bar graphs showing the percentage change of synaptic gene mRNA in hiPSC-N infected with *SMARCC2* shRNA lentivirus, compared to hiPSC-N infected with scrambled shRNA lentivirus. $n = 10$ cultures/2 lines/group, *SMARCC2*: $p < 0.001$; *GABBR2*: $p = 0.0011$; *GABBR1*: $p = 0.03$; *GRIA2*: $p = 0.0002$; *GRIA3*: $p = 0.015$; *GRIN2B*: $p = 0.0076$; *SLC1A3*: $p < 0.001$; *VAMP3*: $p < 0.001$; *SNAP29*: $p = 0.0026$; *SYT2*: $p = 0.02$. One sample t-test. All data are shown as mean ± SEM, $^*p < 0.05$, $^{**}p < 0.01$, $^{***}p < 0.001$.

decreased by *SMARCC2* knockdown in hiPSC-N, including GABA-related genes *GABBR1/2*, glutamate-related genes *GRIA2/3*, *GRIN2B, SLC1A3*, and presynaptic transmitter release-related genes *VAMP3*, *SNAP29*, *SYT2*. These results from human cells have corroborated with the mouse data.

Smarcc2 deficiency in mouse PFC diminishes inhibitory and excitatory synaptic transmission

Given the downregulation of synaptic genes by *Smarcc2* deficiency, we next performed whole-cell patch-clamp recordings of PFC layer V pyramidal neurons, the principal cortical output cells controlling executive function [29, 30] and exhibiting the most prominent impairment in ASD [23]. As shown in Fig. 5a, Smarcc2^{KD} mice had a significant decrease of the amplitude and frequency of spontaneous inhibitory postsynaptic current (sIPSC), compared to control mice. Furthermore, Smarcc2^{KD} mice exhibited a marked reduction in the input/output curve of IPSC evoked by a series of stimulation intensities (Fig. 5b). Paired-pulse ratio (PPR) of evoked IPSC, a measure of presynaptic GABA release, was not significantly changed (Fig. 5c). In parallel experiments

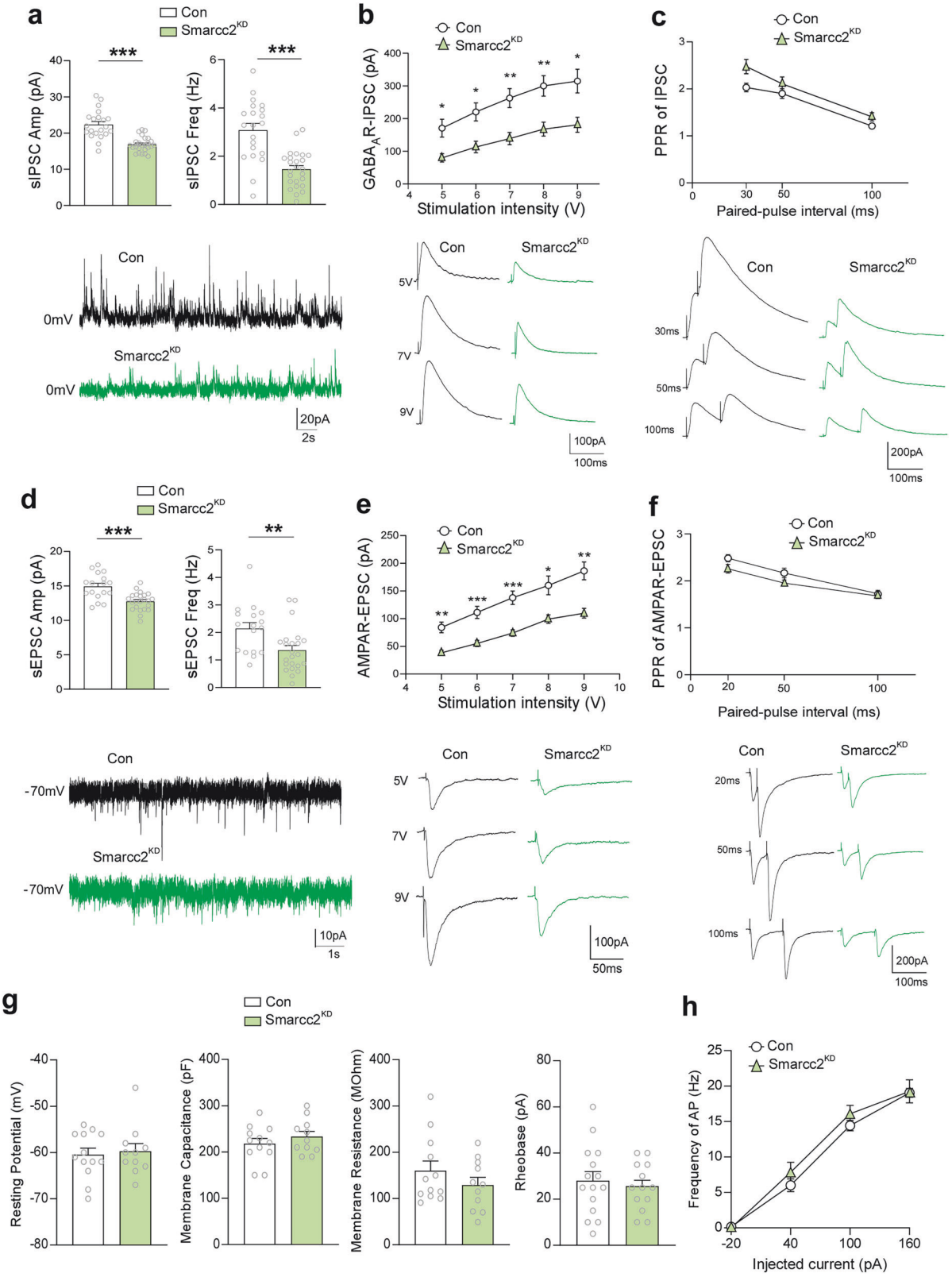

examining excitatory transmission, Smarcc2^{KD} mice had a significant decrease of spontaneous excitatory postsynaptic current (sEPSC) amplitude and frequency (Fig. 5d). Also, Smarcc2^{KD} mice exhibited the decreased EPSC evoked by various stimuli (Fig. 5e), while PPR of evoked EPSC was largely unchanged (Fig. 5f). In addition, no changes were observed in the resting membrane potential, membrane capacitance, membrane resistance, and rheobase in PFC pyramidal neurons of Smarcc2^{KD} mice (Fig. 5g). Input-output relationship of the frequency of action potentials evoked by injected currents was also comparable

Fig. 5 *Smarcc2* deficiency impairs GABAergic and Glutamatergic transmission of PFC pyramidal neurons. a–c Plots of spontaneous IPSC (sIPSC) amplitude and frequency (**a**), input-output curves of evoked IPSC (**b**), and paired-pulse ratio (PPR) of IPSC (**c**) in PFC pyramidal neurons from control vs. Smarcc2^{KD} mice. a, $n = 21–25$ cells/5–6 mice/group, $t_{29.3} = 5.9$ (amp), $t_{31.3} = 5.2$ (freq), $p < 0.001$, t-test; b, $n = 16–17$ cells/5 mice/group, $F_{1,31(genotype)} = 12.5$, $p = 0.0013$, $p < 0.05$, $p < 0.01$, two-way rmANOVA; c, $n = 15–16$ cells/5 mice/group, $F_{1,29(genotype)} = 5.0$, $p = 0.033$, two-way rmANOVA. Inset: representative sIPSC and eIPSC traces. **d–f** Plots of spontaneous EPSC (sEPSC) amplitude and frequency (**d**), input-output curves of evoked EPSC (**e**), and PPR of EPSC (**f**) in PFC pyramidal neurons from control vs. Smarcc2^{KD} mice. d, $n = 17–23$ cells/5–6 mice/group, amp: $t_{38} = 4.3$, $p < 0.001$; t-test; freq: $U = 100$, $p < 0.01$, M-W test; e, $n = 15–16$ cells/5 mice/group, $F_{1,29(genotype)} = 20.9$, $p < 0.001$, two-way rmANOVA; f, $n = 18–19$ cells/5 mice/group, $F_{1,35(genotype)} = 3.0$, $p = 0.09$, two-way rmANOVA. Inset: representative sEPSC and eEPSC traces. **g** Resting membrane potential (Vm), membrane capacitance (Cm), membrane resistance (Rm), and rheobase of PFC pyramidal neurons from control vs. Smarcc2^{KD} mice. $n = 11–15$ cells/3–4 mice/group, Vm: $t_{22} = 0.3$, $p = 0.7$; Cm: $t_{21} = 1.0$, $p = 0.4$; Rm: $t_{21} = 1.1$, $p = 0.3$; rheobase: $t_{26} = 0.5$, $p = 0.6$, t-test. **h** Frequency of action *p*otential (AP) in response to injected currents in PFC pyramidal neurons from control vs. Smarcc2^{KD} mice. $n = 12–19$ cells/4–5 mice/group, $F_{1,29(genotype)} = 0.85$, $p = 0.36$, two-way rmANOVA. Data are shown as mean ± SEM, $^{*}p < 0.05$, $^{**}p < 0.01$, $^{***}p < 0.001$.

between the two groups (Fig. 5h), indicating the preservation of passive membrane properties and overall intrinsic excitability. These data suggest that GABAergic synaptic inhibition and glutamatergic synaptic excitation are compromised by *Smarcc2* deficiency, probably due to the attenuated expression of synaptic genes.

Smarcc2 deficiency induces the reduction of histone acetylation

Among SMARCC2-binding genes involved in ASD, many are histone modifiers, including *EP300*, *ASH1L*, *EHMT1*, *KMT2A*, *SETD1A* (Fig. 1b). Thus, we tested whether *Smarcc2* deficiency might affect histone acetylation and methylation, therefore altering gene expression. In N2A cells transfected with *Smarcc2* shRNA, we found a significant decrease of the level of H3K9ac and H3K27ac, while H3K27me3 and H3K4me3 levels were unchanged (Fig. 6a). Similarly, significantly decreased H3K9ac and H3K27ac levels were found in PFC of mice injected with *Smarcc2* shRNA AAV, without significant changes in H3K27me3 and H3K4me3 levels (Fig. 6b).

With the decrease of histone acetylation by *Smarcc2* deficiency, we next examined the potential interaction between Smarcc2 and histone deacetylases (HDACs) using co-immunoprecipitation (Co-IP) assays. As shown in Fig. 6c, Smarcc2 had a strong binding with HDAC2, and this association was decreased in Smarcc2^{KD} mice, which may free HDAC2 to deacetylate H3, resulting in reduced H3K9ac and H3K27ac.

The global reduction of histone acetylation by *Smarcc2* deficiency prompted us to test whether synaptic genes had reduced histone acetylation at their promoters in Smarcc2^{KD} mice, which led to their transcriptional downregulation. To test this, we conducted chromatin immunoprecipitation (ChIP) assays to examine H3K9ac occupancy at the promotor region of *Slc1a3* (EAAT1), *Slc6a1* (GAT1), and *Slc32a1* (VGAT), representative synaptic genes with diminished expression in Smarcc2^{KD} mice. Primers were designed at the TSS region of these genes with strong H3K9ac occupancy from ChIP-seq landscapes (Fig. 6d). ChIP-PCR revealed a significant decrease of H3K9ac enrichment at *Slc1a3*, *Slc6a1*, and *Slc32a1* promoters in Smarcc2^{KD} mice, compared to controls (Fig. 6e), suggesting that *Smarcc2* deficiency-induced downregulation of these synaptic genes may be attributable to the reduced histone acetylation.

HDAC inhibitor mitigates cognitive and synaptic deficits in *Smarcc2*-deficient mice

With the identified reduction of histone acetylation by *Smarcc2* knockdown, we next investigated whether elevating histone acetylation with HDAC inhibition could ameliorate phenotypes of Smarcc2^{KD} mice. The potent and brain-permeable class I HDAC inhibitor, romidepsin, was administered as we previously described (0.25 mg/kg, i.p. once daily for 3 days) [6, 31]. Immunostaining of H3K9ac demonstrated that the reduced H3K9ac fluorescence intensity in PFC of Smarcc2^{KD} mice was significantly restored following romidepsin treatment (Fig. 7a). Behavioral assays indicated that romidepsin treatment significantly improved the performance of Smarcc2^{KD} mice in spontaneous T maze working memory tests, as evidenced by the increased correctness across different trials (Fig. 7b).

To find out potential mechanisms underlying the behavioral effects of romidepsin, we examined its impact on synaptic gene expression. As shown in qPCR profiling (Fig. 7c), while romidepsin treatment did not change *Smacc2*, it significantly or partially rescued several GABA- and glutamate-related genes diminished in Smarcc2^{KD} mice (*Gad1*, *Slc32a1*, and *Slc1a3*).

RNA-seq analysis further revealed that, among 653 down-regulated genes by *Smarcc2* knockdown, 136 genes were elevated by romidepsin treatment (Supplementary Table 5, 4.54 fold over-enrichment, hypergeometric *p*-value: 2.56E–53). Among these romidepsin-restored genes, 18 were synaptic genes (Fig. 7d), including *Syt6* and *Syt9* (encoding synaptotagmin 6 and 9) involved in Ca^{2+}-dependent exocytosis of synaptic vesicles.

Next, we examined whether romidepsin treatment could ameliorate synaptic dysfunction induced by *Smarcc2* knockdown. As shown in Fig. 7e–g, the profoundly decreased $GABA_A$R-IPSC amplitudes in PFC pyramidal neurons of Smarcc2^{KD} mice were markedly increased by romidepsin treatment, compared to saline treatment, although the rescuing effect was partial. On the other hand, the diminished AMPAR-EPSC amplitudes in PFC pyramidal neurons of Smarcc2^{KD} mice were elevated to near control levels by romidepsin treatment. These data indicate that HDAC inhibition can significantly improve inhibitory and excitatory synaptic transmission in *Smarcc2*-deficient mice.

Finally, we examined the impact of romidepsin treatment on synaptic gene expression in human hiPSC-derived cortical neurons. As shown in the landscape of SMARCC2, HDAC2 and H3K27ac ChIP-seq data, they had overlapping enrichment at promoter regions of synaptic genes, such as *VAMP3, SNAP29* (Fig. 7h), *GRIA2, SLC1A2, GAD1, GABBR1* (Figure S7), further suggesting that SMARCC2 and HDAC2 may converge on these loci to regulate gene expression. Our qPCR profiling indicated that the diminished synaptic genes in Smarcc2^{KD} hiPSC-N, such as *VAMP3, SNAP29, and SLC1A3*, were significantly elevated by romidepsin treatment, consistent with the rescuing effect of romidepsin in PFC of Smarcc2^{KD} mice.

DISCUSSION

Based on our data, we propose a model revealing the potential link of Smarcc2 to ASD/ID (Fig. 8). SMARCC2 and HDAC2 exert opposing, competitive effects at shared regulatory regions of target genes. In normal state, the SMARCC2-containing BAF complex promotes chromatin opening through nucleosome repositioning or ejection, thereby increasing accessibility for transcription factors and RNA polymerase and facilitating the expression of synaptic genes [32]. In this context, BAF activity counteracts and predominates over HDAC-mediated repression. Under *Smarcc2*-deficient conditions, BAF complex activity is

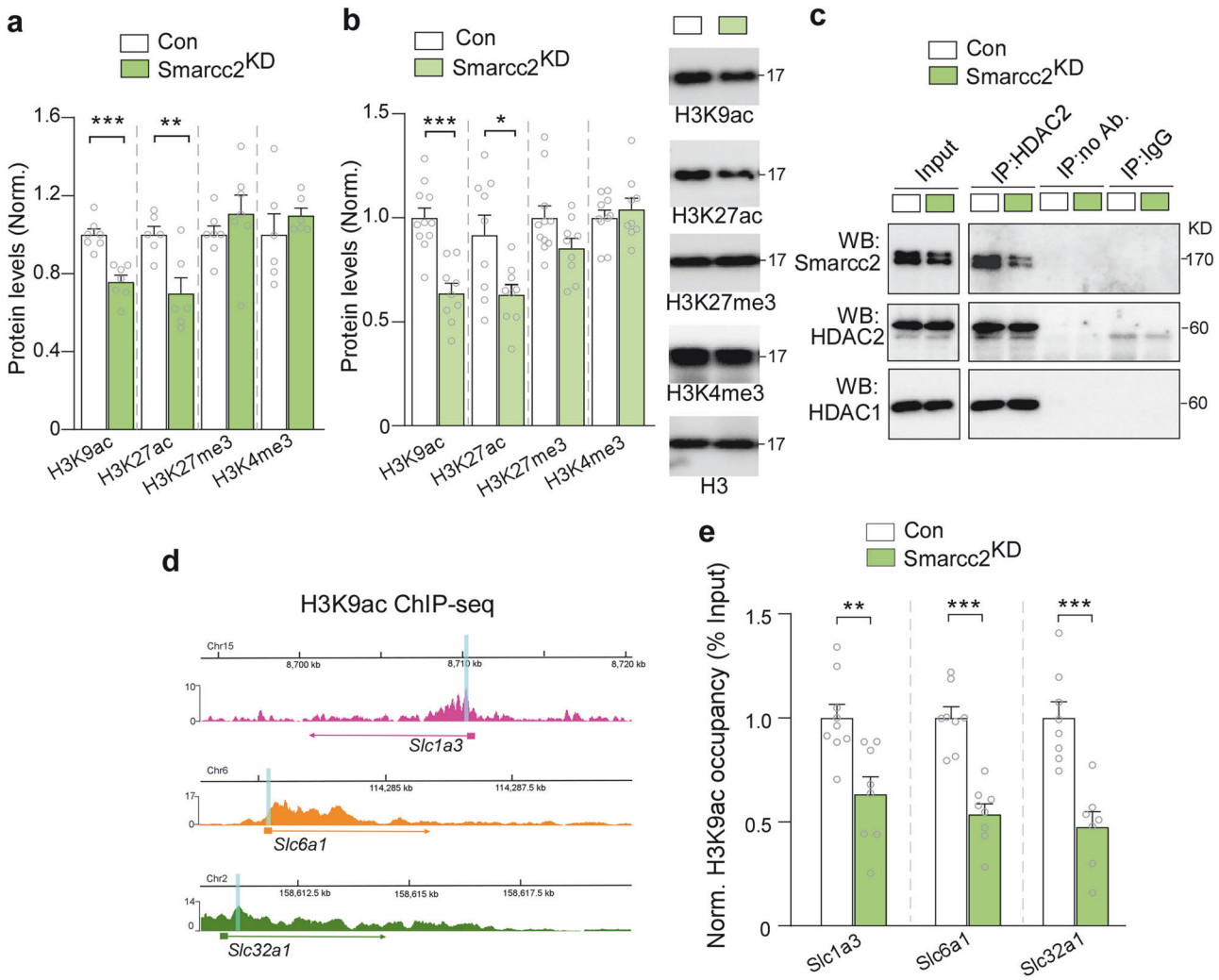

Fig. 6 ***Smarcc2* deficiency reduces global histone acetylation, diminishes HDAC2-Smarcc2 binding, and decreases H3K9ac occupancy at synaptic gene promotors. a, b** Bar graphs showing the level of H3K9ac, H3K27ac, H3K27me3, and H3K4me3 in N2A cells transfected with control vs. Smarcc2 shRNA (**a**) or PFC tissue from mice injected with control vs. *Smarcc2* shRNA AAV (**b**). a, $n = 6$–7 cultures/group, H3K9ac: $t_{12} = 5.5$, $p < 0.001$; H3K27ac: $t_{10} = 3.3$, $p = 0.008$; b, $n = 9$–11 mice/group, H3K9ac: $t_{18} = 5.3$, $p < 0.001$; H3K27ac: $t_{16} = 2.7$, $p = 0.016$. **c** Representative immunoblots of co-IP experiments showing HDAC2-bound Smarcc2 in control vs. Smarcc2^{KD} mice. Anti-HDAC2 was used for IP, anti-Smarcc2, anti-HDAC2 and anti-HDAC1 was used for blotting. No antibody and IgG were used as negative controls for IP. **d** Diagram showing H3K9ac occupancy at *Slc1a3, Slc6a1*, and *Slc32a1* promotor regions, including the location of primers used in ChIP-PCR assays (light blue rectangular area). **e** ChIP assay data showing differential H3K9ac levels at *Slc1a3, Slc6a1* and *Slc32a1* promoters in the PFC of control vs. Smarcc2^{KD} mice. $n = 7$–9 mice/group. *Slc1a3*: $t_{15} = 3.5$, $p = 0.003$; *Slc6a1*: $t_{14} = 6.3$, $p < 0.001$; *Slc32a1*: $t_{13} = 4.8$, $p = 0.0003$, t-test. All data are shown as mean ± SEM. *$p < 0.05$, **$p < 0.01$, ***$p < 0.001$.

diminished, leading to reduced chromatin accessibility. As a result, HDAC activity becomes more dominant, causing decreased histone acetylation and reduced expression of GABA- and glutamate-related synaptic genes. Consequently, inhibitory and excitatory synaptic transmission in PFC is compromised, leading to cognitive impairment. These synaptic and behavioral deficits can be ameliorated by HDAC inhibition, providing a therapeutic strategy for *SMARCC2*-associated neurodevelopmental disorders.

Smarcc2 is recognized as a key scaffold protein involved in the assembly and regulation of BAF chromatin remodeling complexes [33], which modulate genomic architecture by sliding or ejecting nucleosomes [34]. In humans, *SMARCC2* mutations include missense, truncating, and splice-site variants distributed across multiple key functional domains, such as SWIRM, SANT, and SMARCC_N regions, which mediate DNA interaction, histone binding, and protein–protein interactions within the BAF complex [16]. Disruption of BAF complexes has been frequently associated with human cancers [35] and developmental disorders [36]. Here, we found a significant reduction of SMARCC2 in PFC of a cohort of idiopathic ASD patients. To investigate the functional consequence of *Smarcc2* deficiency, we knocked down *Smarcc2* in PFC of adolescent mice, and found the impaired working memory, which is also impaired in ASD patients [37]. This cognitive deficit aligns with phenotypic observations in humans carrying *de novo SMARCC2* mutations [16, 17], supporting the causal link of *SMARCC2* haploinsufficiency to ASD/ID [2]. Although social communication deficit is a core symptom of ASD, mice with *Smarcc2* deficiency in PFC had normal social preference in our behavioral assays. Spatial and temporal restriction of *Smarcc2* knockdown may underlie the observed phenotype, because social behaviors are mediated by distributed circuits, including PFC, amygdala, nucleus accumbens, anterior cingulate cortex, hypothalamic circuit [38–41], and earlier developmental stages are important for social circuit formation [42]. Moreover, the three-chamber test may not detect more subtle alterations in social behavior. Nevertheless, as only a subset (~35%) of individuals with

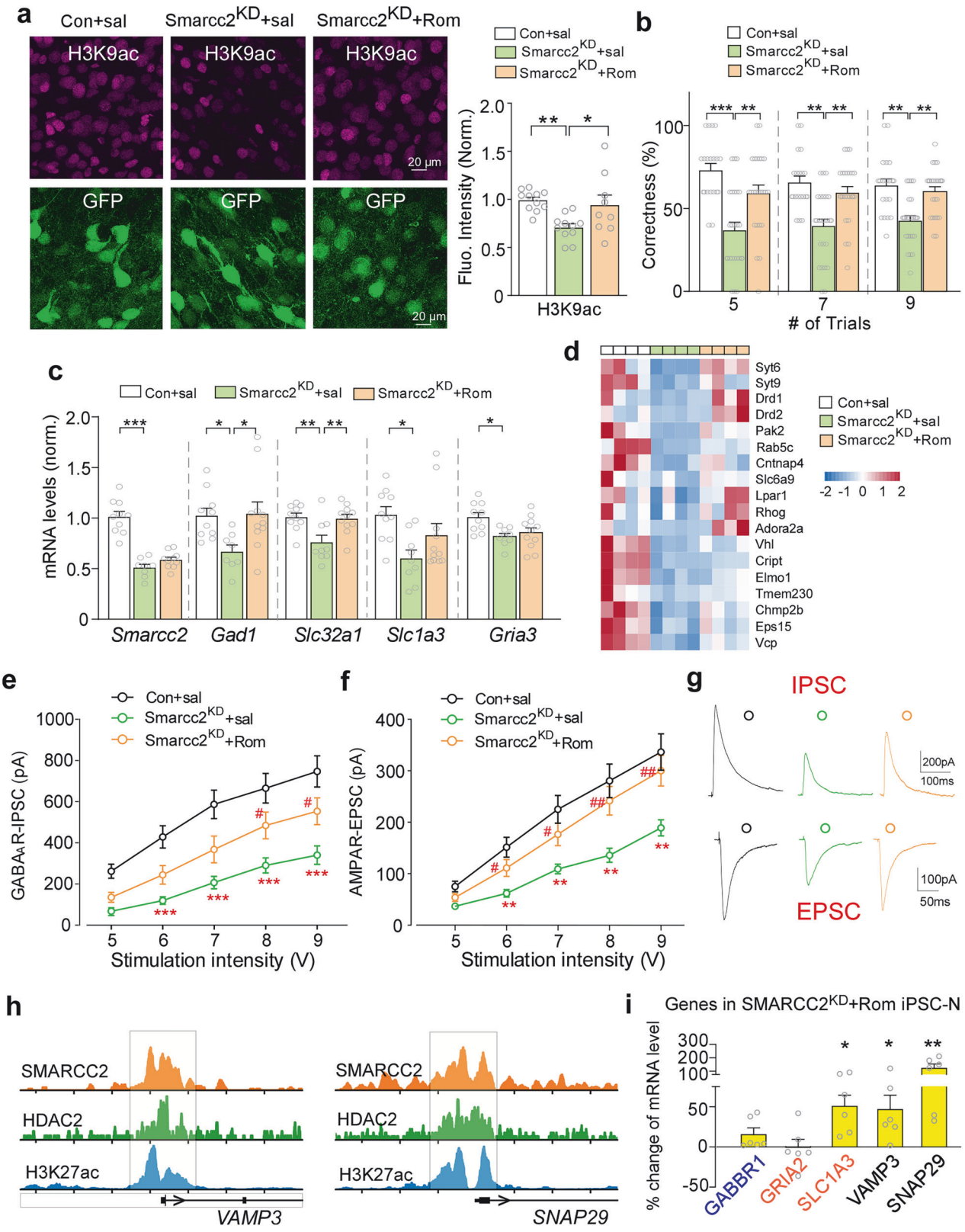

SMARCC2 variants exhibit autistic behaviors, it suggests that *Smarcc2* deficiency may not always produce social deficits.

Accumulating evidence indicates that synaptic dysfunction is a key pathogenic factor in ASD [6, 9, 22, 43–45]. Our transcriptomic analyses revealed that *Smarcc2* deficiency in PFC of adolescent mice significantly downregulated synaptic genes, particularly those involved in chemical synaptic transmission. Consistently, we found that embryonic (E16.5) cells from *Smarcc1/2* double knockout mice [18] also had synaptic genes enriched in the downregulated gene set. In agreement with this, deep single-

Fig. 7 HDAC inhibitor treatment of Smarcc2^{KD} mice normalizes H3K9ac levels, rescues working memory deficits, and restores synaptic gene expression and synaptic function. a Representative confocal images (63×) showing H3K9ac immunostaining (magenta) and quantification of H3K9ac fluorescence intensity in control vs. Smarcc2^{KD} mice treated with saline or romidepsin. Scale bars: 20 µm. $n = 9$–11 images/4 mice/group, $F_{2,28} = 6.4$, $p = 0.0051$, one-way ANOVA. **b** Bar graph depicting the percentage of correct response in spontaneous T maze alternation tests of the 3 groups of mice. $n = 20$–25 mice/group. Percent Correctness, 5 trials: $F_{2,56} = 12.1$, $p < 0.001$, one-way ANOVA; 7 trials: KW = 13.7, $p = 0.001$; 9 trials: KW = 15.1, $p < 0.001$, K-W test. **c** Bar graph showing the mRNA level of *Smarcc2* and synaptic genes in the 3 groups of mice. $n = 8$–11 mice/group. *Smarcc2*: $F_{2,25} = 46.6$, $p < 0.001$; *Gad1*: $F_{2,26} = 4.5$, $p = 0.02$; *Slc32a1*: $F_{2,27} = 7.1$, $p = 0.003$; *Gria3*: $F_{2,25} = 5.4$, $p = 0.01$, one-way ANOVA; *Slc1a3*: KW = 9.0, $p = 0.01$, K-W test. **d** Heatmap showing the expression levels of synaptic genes in the 3 groups of mice from RNA-seq data. **e, f** Plots of input-output curves of evoked IPSC (**f**) or EPSC (**g**) in pyramidal neurons from control and Smarcc2^{KD} mice treated with saline or romidepsin. IPSC: $F_{2,31(group)} = 11.6$, $p = 0.0002$, $n = 10$–12 cells/3–4 mice/group; EPSC: $F_{2,33(group)} = 7.9$, $p = 0.0016$, $n = 11$–14 cells/3–4 mice/group, two-way rmANOVA, *: Smarcc2^{KD}+sal vs. Con+sal; #: Smarcc2^{KD}+rom vs. Smarcc2^{KD}+sal. **g** Representative eIPSC and eEPSC traces. **h** SMARCC2, HDAC2 and H3K27ac ChIP-seq landscapes on *VAMP3* and *SNAP29* promoters. **i** Bar graphs showing the percentage change of synaptic gene mRNA in Smarcc2^{KD} hiPSC-N treated with romidepsin, compared to Smarcc2^{KD} hiPSC-N treated with vehicle. *SLC1A3*: $p = 0.012$; *VAMP3*: $p = 0.042$; *SNAP29*: $p = 0.0093$, One sample t-test. All data are shown as mean ± SEM, $^{*}p < 0.05$, $^{**}p < 0.01$, $^{***}p < 0.001$, $^{\#}p < 0.05$, $^{\#\#}p < 0.01$.

nucleus RNA sequencing of postmortem human brains revealed that the loss of synaptic genes in pre- and postsynaptic compartments of excitatory and inhibitory neurons was the most prominent change in ASD patients [46]. Quantitative PCR confirmed the reduction of inhibitory (*Gad1*, *Slc6a1*, *Slc32a1*) and excitatory (*Slc1a3*, *Gria3*) synaptic genes in *Smarcc2*-deficient mice. Not all DEGs identified by RNA-seq were validated by qPCR. The discrepancy could be due to biological variability between independent cohorts or differences in statistical sensitivity between the two approaches. However, despite differences at the individual gene level, both approaches consistently indicate dysregulation of synaptic transmission-related pathways, supporting the overall biological conclusion. In agree with this, *SMARCC2* knockdown in human hiPSC-N led to the reduction of synaptic genes. Electrophysiological recordings further revealed the significantly diminished GABAergic and glutamatergic synaptic currents in PFC pyramidal neurons of *Smarcc2*-deficient mice. These data have for the first time uncovered the critical role of *Smarcc2* in maintaining synaptic function of mature neurons.

While BAF complexes are known to modulate chromatin structure, the precise epigenetic mechanisms by which Smarcc2 regulates synaptic genes remain unclear. We found that Smarcc2 bound to HDAC2, and Smarcc2 knockdown led to the decreased histone acetylation (H3K9ac and H3K27ac) without significantly affecting other histone marks (H3K27me3 and H3K4me3). H3K9ac and H3K27ac are associated with active transcription and play a pivotal role in development [47, 48]. Embryonic cells from *Smarcc1/2* double knockout mice also had the reduced H3K9ac, however, a dramatic increase of H3K27me3, a gene repression marker [49], was thought to underlie the impact of *Smarcc1/2* loss on genes involved in early development in these embryonic cells [18]. Our ChIP-PCR results on the reduced H3K9ac occupancy at promoters of downregulated synaptic genes in *Smarcc2*-deficient mice provide further evidence on the role of histone acetylation in Smarcc2 regulation of synaptic gene expression.

Smarcc2 knockdown reduced the interaction between Smarcc2 and HDAC2, which may lead to the enhanced association between HDAC2 and histone H3, causing the reduced histone acetylation. One therapeutic strategy for *Smarcc2*-deficient mice is to elevate histone acetylation via HDAC inhibition. Dysregulated HDAC activity has been implicated in both ASD and ID due to its impact on neurodevelopmental gene expression [50, 51]. HDAC inhibitors have been used in treating various ASD/ID models [5, 6, 52–54]. Here we found that a short treatment of *Smacc2*-deficient mice with romidepsin, a selective class I HDAC inhibitor, restored H3K9ac levels, improved working memory, and partially normalized synaptic genes expression and synaptic function. These findings underscore the therapeutic potential of HDAC inhibitors in ameliorating phenotypes associated with *Smarcc2* haploinsufficiency.

The study has several limitations for consideration. Despite our finding on the reduced SMARCC2 protein level in the nuclear fraction of PFC from the tested ASD postmortem samples, it is still unclear whether the lower expression of SMARCC2 is a convergent phenotype of ASD. RNA-seq data show a significant reduction of *SMARCC2* mRNA in the cortex of humans with dup15q syndrome, but not idiopathic ASD [55]. We focused the molecular and physiological measurements on medial PFC, because it is a key region consistently implicated in ASD [21–23]. We knocked down *Smarcc2* in adolescent mice, because our goal is to reveal the role of Smarcc2 on synaptic gene expression and synaptic function in mature PFC neurons and bypass the influence of Smarcc2 on early neural proliferation and CNS development [18, 19, 56]. However, such a *Smarcc2*-deficienct mouse model has spatial and temporal limitations and does not recapitulate the broader pathogenic consequences of germline *SMARCC2* loss-of-function mutations in humans. Future studies will be needed to define Smarcc2 function across brain regions and time windows, determine whether nucleosome repositions or remodeling activity are altered by *Smarcc2* deficiency, and assess the impact of *Smarcc2* deficiency on chromatin accessibility with ATAC-seq.

EXPERIMENTAL PROCEDURES

Ethics approval

All animal studies were conducted with the approval of the Institutional Animal Care and Use Committee (IACUC) at the State University of New York at Buffalo (IACUC ID: PROTO202000049). All methods were performed in accordance with the relevant guidelines and regulations.

Animals, human postmortem tissue and reagents

Five-week-old C57BL/6J mice (Strain #: 000664, The Jackson Lab) of both sexes were used in this study. Frozen human postmortem tissue (Brodmann area 9) from normal control and patients with ASD were provided by NIH Neuro BioBank (Supplementary Table 6). ASD patients (5 Males, 2 Females) were 4–19 years old (mean age: 11.7 years old), while age- and sex-matched control subjects (7 Males, 2 Females) were 6–19 years old (mean age: 13.2 years old). Tissue was stored in −80 °C until later protein extraction.

To knockdown *Smarcc2* in mouse medial PFC, a short hairpin RNA (shRNA) sequence (CCCGATAGTTGATCCTGAGAA) was cloned into GFP-tagged adeno-associated virus (AAV) vector (Addgene) under the control of U6 promotor. Viral particles (8×10^{14} vg/ml) were produced by the viral core center of Emory University. Romidepsin (rom, Selleckchem, S3020) was prepared in DMSO and stored at −20 °C at the stock concentration of 1 mg/ml. Prior to use, the stock solution was diluted with saline.

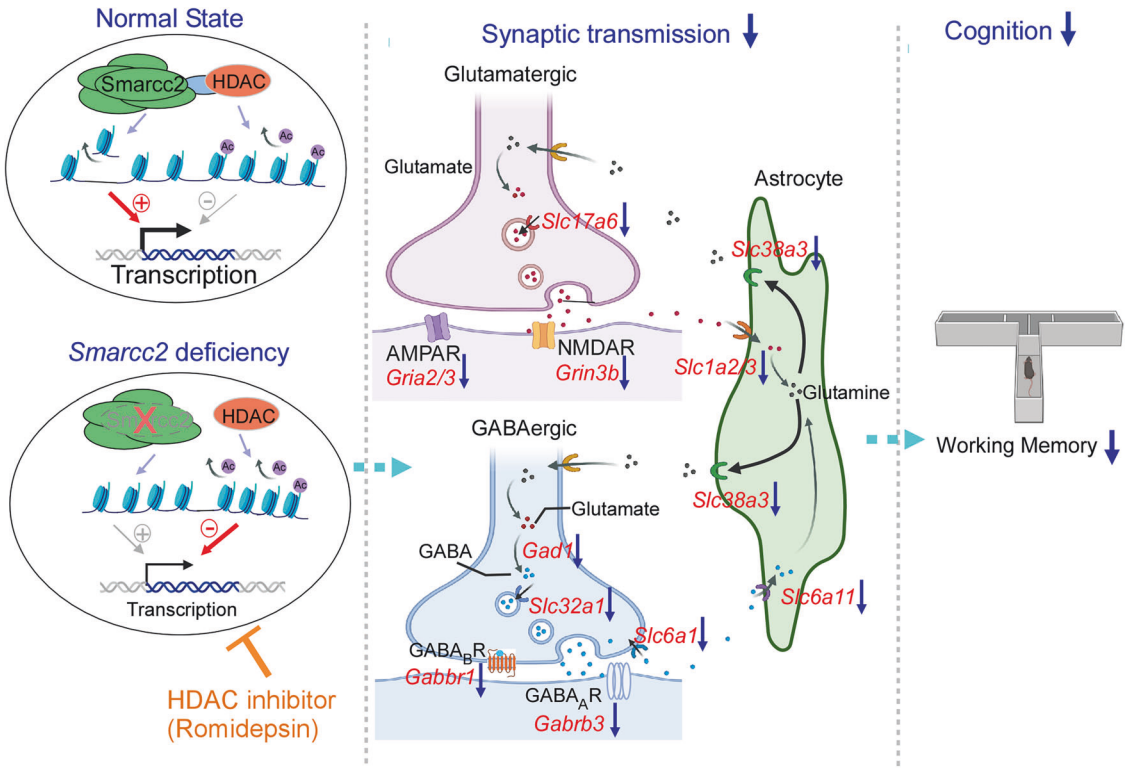

Fig. 8 A schematic model illustrating the impact of Smarcc2 deficiency and a therapeutic strategy. Knockdown of Smarcc2, a core subunit of chromatin remodeler BAF complex, decreases the level of histone acetylation, leading to the reduced expression of synaptic transmission-related genes in both glutamatergic and GABAergic synapses. The resulting attenuation of excitatory and inhibitory synaptic transmission leads to cognitive deficits (WM). Treatment with the class I HDAC inhibitor romidepsin restores H3K9ac levels and rescues synaptic genes expression and synaptic function, leading to cognitive improvement.

Animal surgery

In brief, mice were anaesthetized with ketamine/xylazine (100/10 mg/kg, i.p.). After exposing the skull through a small incision, a small burr hole was drilled in each hemisphere at the appropriate coordinates relative to bregma for injection. Stereotaxic AAV injections were performed in the medial PFC (2.0 mm anterior to bregma; 0.3 mm lateral; 2.0 mm dorsal to ventral; 1 µl per hemisphere) [9, 57]. The working AAV titer is 4×10^{13} vg/ml. The injections were administered with a Hamilton syringe (gauge 34) at a speed of 0.1 µl/min, and the needle was kept in place for an additional 10 min.

Behaviors

All behavioral tests were conducted 2 weeks post-stereotaxic injection. All the tests were performed between 10 a.m. and 6 p.m. under dim lighting conditions. Mice were acclimated to the testing room for 1 h before tests. Any-maze software was used to track and record behavioral data. To minimize olfactory interference, testing equipment was cleaned with 70% ethanol between different animals. Additionally, to avoid the potential disturbance of gender, male and female mice were tested separately.

Spontaneous T maze was used to assess working memory, with modification based on the protocol [24, 58]. The T-shaped maze consists of a start area (12"Lx5.5"Wx6"H) and two arms (23"Lx5.5"Wx6"H). Mice were initially placed in the start area for 30 s, after which they were allowed to choose either arm within 2 min. Upon complete entry into an arm, the mouse was confined within that arm for 30 s before being returned to the start area. If a mouse failed to exit an arm within 10 s, a clean paper was used to gently guide it out. The procedure was repeated for 10 trials. A correct choice was defined as selecting an arm opposite to the chosen one in the previous trial. The percentage of correctness was calculated from trial 2 to trail 10.

Barnes Maze (BM) was employed to evaluate the spatial memory. As described previously [27, 57], mice were placed at the edge of a round arena containing 8 evenly spaced holes. Three different visual cues were placed on the surrounding walls. The mouse faced the opposite direction of the correct hole, which has an escape box attached underneath. A bright light overhead was used as an aversive stimulus. After 5-min habituation, the mouse underwent two training sessions, each lasting 5 min, with a 5-min rest interval in the holding cage between sessions. After 15 min break, the mouse was put back on the arena for the final test in which the escape box was removed. Time spent exploring the correct hole (T1) and incorrect holes (T2) were recorded. T1/T2 index was calculated to evaluate the spatial memory.

Grooming was used to test repetitive behavior [25]. The mouse was put in a holding cage individually and allowed to explore for 30 min. A camera was used to record the whole session. The grooming time and frequency were counted manually for the last 10 min.

Social preference test was performed to assess sociability. As described previously [26, 59], a three-chamber apparatus with two inverted cups in the side chambers was used. One day before the test, the mouse was put in the center chamber and allowed to explore the three chambers with two empty cups for 10 min (habituation). On the test day, two identical non-social objects (paper balls) were placed underneath the inverted cups in the three-chamber apparatus for the mouse to explore (10 min). Following a 5-min rest in the holding cage, the mouse was put back in the three chambers with two cups containing one non-social object (wooden block) and one social object (sex- and age-matched mouse) to explore for another 10 min. The time interacting with social (T_{soc}) and non-social objects (T_{NS}) were

recorded. (T_{soc}-T_{NS})/ (T_{soc}+T_{NS}) was calculated as social preference index.

Elevated plus maze (EPM) was utilized to assess anxiety. As described preciously [27], mice were placed at the center of a plus-shaped arena, facing an open arm and allowed to explore freely for 10 min. Time spent in the open arms and closed arms, latency to the open arms, and the total distance traveled were recorded.

Light and dark box test was used to evaluate anxiety [60]. The apparatus consisted of a light and a dark chamber of equal size (14.5"Lx10.5"Wx13"H). Mice were placed in the light box, facing away from the door. The time spent in the light box and the frequency to enter the light box within 10 min was recorded.

Open Field (OF) was conducted to assess anxiety and locomotor activity. As described previously [27], the mouse was placed in the center of a rectangular arena with opaque walls and allowed to explore freely for 10 min. The center area was defined as half length and width of the arena. Total distance traveled and time spent in the center area were recorded.

Resident-intruder (RI) test was used to evaluate aggression [31], Briefly, mice were single housed for 1 day before test. During the test, an intruder (an unfamiliar, group-housed, same sex WT mouse of 5–15% lighter) was introduced into the resident's home cage for 10 min. Each intruder was used only once. Aggressive behavior of the resident mouse against the intruder was scored. The duration and frequency of aggression, as well as the total social interactions between the resident mouse and the intruder, were counted manually.

Western blot

Nuclear protein extraction was performed as we previously described [9] with modifications. Briefly, GFP-positive PFC tissue was dissected under a microscope with fluorescence adapter system (Avantor Science Central, 77463-320). Tissues were homogenized with 250 µl hypotonic buffer with protease inhibitor cocktail and 1 mM PMSF, followed by incubation on ice for 15 min. Subsequently, 12.5 µl of 10% NP-40 was added and the mixture was vortexed for 10 s. The homogenate was centrifuged at 3000 g for 10 min at 4 °C. The nuclear pellet was resuspended in filtered 1% SDS containing protease inhibitor cocktail and 1 mM PMSF. All samples were normalized to the same concentration and boiled in 4x SDS loading buffer for 10 min. Proteins were separated using 6 and 12% SDS-polyacrylamide gels. A total of 10 µg proteins was loaded for target proteins, while 5 µg was used for Histone H3. Western blotting was performed using antibodies against Smarcc2 (Cell Signaling, 12760, 1:1000), Smarcc1 (Cell Signaling, 11965, 1:1000), H3K9ac (Cell Signaling, 9649, 1:1000), H3K27ac (Cell Signaling, 8173, 1:1000), H3K27me3 (Cell Signaling, 9733, 1:1000), H3K4me3 (Abcam, ab8580, 1:1000) and Histone H3 (Cell Signaling, 4499, 1:1000).

Real-time RT-PCR

Total RNA was extracted using Trizol reagent (Invitrogen, 15596026). cDNA was synthesized using the iScriptTM cDNA synthesis Kit (Bio-Rad, 1708891). Quantitative real-time PCR was performed using the CFX Connect Real-Time PCR Detection System and iQ™ SYBR® Green Supermix (Bio-Rad, 1708882). GAPDH was used as the housekeeping gene for normalization. Each 20 µl reaction was run in a 96-well PCR plate (Bio-Rad, HSP9601) using the following cycling parameters: 95 °C for 3 min followed by 40 cycles of 95 °C for 15 s, 60 °C for 20 s, and 72 °C for 30 s. Fold changes in the target gene expression were calculated as following: $\Delta Ct = Ct(target) - Ct(GAPDH)$, and $\Delta(\Delta Ct) = \Delta Ct(Smarcc2^{KD}) -$ mean $\Delta Ct(control)$ or $\Delta(\Delta Ct) = \Delta Ct(Smarcc2^{KD}+drug) -$ mean $\Delta Ct(Smarcc2^{KD}+saline)$, and Fold change $= 2^{-\Delta(\Delta Ct)}$. Primers used in qPCR experiments are included in Supplementary Table 7.

Immunohistochemistry

Mice were anesthetized with ketamine/ xylazine and transcardially perfused with phosphate buffered saline (PBS) and 4% fresh prepared paraformaldehyde (PFA) [9]. Brains were post-fixed in 4% PFA overnight, dehydrated in 30% sucrose for 2 days and sectioned coronally (50 µm thickness). After three washes with PBS (10 min each), slices were blocked with 5% BSA containing 0.3% Triton for 2 hr at room temperature. Then slices were incubated overnight at 4 °C with primary antibody against Smarcc2 (Cell Signaling, 12760, 1:1000), H3K9ac (Cell Signaling, 9649; 1:1000) or NeuN (Millipore, MAB377; 1:250). Following three PBS washes (15 min each), slices were incubated with secondary antibodies: Alexa Fluor donkey anti mouse-568 (Invitrogen, A10037; 1:1000) and Alexa Fluor goat anti rabbit-647 (Invitrogen, A21245; 1:1000) for 2 hr at room temperature. Nuclei were counterstained with DAPI (ThermoFisher, D1306, 5 µg/ml) for 30 min at room temperature. Sections were mounted using ProLong™ Diamond Antifade Mountant (Invitrogen, P36970). Images were acquired using 63× objective with a Leica TCS SP8 confocal microscope. Identical imaging conditions and parameters were applied to all specimens using Image J software (version 1.52p, NIH).

Generation and treatment of human hiPSC-derived neurons

Human induced pluripotent stem cells (hiPSCs) from both neurotypical controls and idiopathic ASD patients (4 lines per group with each group comprising 2 males and 2 females, 4–10 years old at sampling) were acquired from the Human Pluripotent Stem Cell Line Repository at the California Institute for Regenerative Medicine (CIRM). These hiPSCs were generated using non-integrating Episomal vectors. All hiPSCs were maintained on gamma-irradiated CF-1 mouse embryonic fibroblasts in DMEM/F12 medium supplemented with knockout serum replacement, β-mercaptoethanol, NEAA, L-glutamine, and FGF2. The human hiPSCs were differentiated to cortical neurons as we described [61]. Briefly, hiPSCs were dissociated to form embryoid bodies (EBs), cultured in suspension in a DMEM/F12 and Neurobasal mix with supplements including N2, B27 (vitamin A-free), NEAA, ascorbic acid, SB431542, dorsomorphin, XAV939, and Cyclopamine. On day 6, EBs were plated on Matrigel-coated plates and maintained for 6 days. At day 12, dorsal cortical progenitors were dissociated with Accutase and plated on polyornithine/Matrigel-coated plates at 5000–10,000 cells/cm^2 in the same medium with Y27632 added for the first 24 h. Cells were passaged again on day 16. From day 18, the medium was changed to Neurobasal with B27 (vitamin A-free), BDNF, GDNF, dcAMP, ascorbic acid, and DAPT to promote cortical neuron differentiation. Half-medium changes were performed every other day, and neurons were cultured until day 60 for experimental use. Immunostaining and qPCR were performed using protocols consistent with those for mouse tissues.

The *SMARCC2* shRNA sequence (CCCAAGAGTATCTTACCTCTA) was obtained from Broad institute (TRCN0000015699) and cloned into the pLKO.1 vector. A scrambled shRNA vector was purchased from Addgene (#1864), using the scrambled shRNA sequence CCTAAGGTTAAGTCGCCCTCG. All plasmid constructs were verified by sequencing. Lentiviruses expressing *SMARCC2* shRNA or scrambled shRNA were produced in 293FT cells using Lipofectamine 2000 (Invitrogen, 11668019) [62]. At day 56, hiPSC-derived neurons were infected with scrambled or *SMARCC2* shRNA lentivirus at a multiplicity of infection (MOI) of 20. After 4 days of infection, neurons (d60) were harvested for RNA extraction. For romidepsin treatment, hiPSC-derived neurons were treated with 50 pM romidepsin on Day 58, DMSO was used as the vehicle control. After 2 days of treatment, hiPSC-derived neurons (D60) were harvested for RNA extraction.

ChIP-seq, RNA-seq and data analysis

Human SMARCC2 ChIP-seq data consisting of bigwig files were obtained via Gene Expression Omnibus (GEO) under the accession number GSM5311593 (Brain BT16 cell line), GSM4837715 and GSM4837716 (Blood Fujioka cell line), GSM5311594 and GSM5311596 (Kidney G401 cell line). Top 2000 target genes with SMARCC2 binding peaks at promoters (+/−1 kb of TSS) were selected using ChIP-Atlas (https://chip-atlas.dbcls.jp) for GO analysis. Human HDAC ChIP-seq data were obtained from GSM803493 (Liver Hep G2 cell line). Human H3K27ac ChIP-seq data were obtained from GSM3752817 (frozen postmortem brain tissue, lateral temporal lobe). Mouse H3K9ac data were obtained from GSE82643 (postnatal 0 day forebrain). ChIP-seq bigwig tracks were examined using the Interactive Genome Browser (IGV: https://igv.org/). Landscape plots were generated using a python pipeline including packages "pyBigWig", "numpy", "pandas", "gtfparse", and "matplotlib".

RNA-seq samples were mouse brain tissues (4 samples (2 M, 2 F)/group, 3 groups, each sample (50 mg) contained the dissected GFP-positive PFC region pooled from 3 mice), or hiPSC-derived neurons (4 lines (2 M, 2 F)/group, 2 groups). Total RNA was extracted using the same method as described in the real-time RT-PCR section. RNA-seq libraries were prepared using the TruSeq Stranded Total RNA Plus Ribo-Zero Kit (Illumina) and sequenced on the HiSeq 2500 platform (Illumina) at LC Sciences. Raw paired-end FASTQ reads were cleaned with cutadapt (v. 2024.10.0) and aligned to the *Mus musculus* reference genome (mm10) using HISAT2 (v. 2.2.1). Transcripts assembly of each individual sample, merging and gene level expression counts were quantified using StringTie (v. 2.2.3) and offcompare (v. 0.12.6). Differential gene expression analysis was conducted using DESeq2 (v. 3.2). For hiPSC-Neuron RNA-seq data, DEGs were identified based on $P \leq 0.05$ relative to controls. For mouse RNA-seq data, DEGs were identified based on a fold change (FC) ≥ 1.2 and $P_{adj.} \leq 0.05$ relative to controls.

Biological Processes Gene ontology (GO) analysis was performed using EnrichR (https://maayanlab.cloud/Enrichr/) [63]. Overlap of genesets was done using InteractiVenn (https://www.interactivenn.net/) [64]. Protein-protein interaction (PPI) analysis was performed using String database (https://String-db.org) [65]. Genes were classified into categories (when applicable) with the String-db's Cytoscape (StringApp) plugin. Hub genes were identified, and interactome networks were generated using CytoHubba (v. 0.1) with the maximum clique centrality method. Volcano plots, heatmaps and GO bar plots were generated using ggplot2 (v. 3.5.1). Synaptic specific gene ontology was done using SynGO exported onto a sunburst plot (https://www.syngoportal.org/).

Electrophysiological recordings of brain slices

The whole-cell voltage-clamp recording technique was used to measure synaptic currents in slices as previously described [6, 9, 31, 66]. Mice were decapitated after inhaling isoflurane and the brain was quickly removed, iced, and coronally cut into 300 or 350 µm slices with a vibratome (Leica VP1000S, Leica Microsystems Inc, Germany) in an ice-cold sucrose solution. The slices were incubated in artificial cerebrospinal fluid (ACSF; in mM: 130 NaCl, 26 $NaHCO_3$, 1 $CaCl_2$, 5 $MgCl_2$, 3 KCl, 1.25 NaH_2PO_4, 10 glucose, pH 7.4, 300 mOsm) in 30–35 °C for 1 hr and maintained in room temperature (21 °C), bubbling with 95% O_2 and 5% CO_2. The mouse slices were transferred in a perfusion chamber attached to the fixed stage of an upright microscope (Olympus) and submerged in continuously flowing oxygenated ACSF. In later experiments, an ACSF containing lower Mg^{2+} (1.5 mM) was used to better mimic physiological conditions. Layer V mPFC pyramidal GFP-positive neurons were visualized with a 40X water-immersion lens and recorded with the Multiclamp 700 A amplifier (Molecular Devices, Sunnyvale, CA), Clampex software 9 (Molecular Devices, Sunnyvale, CA) and Digidata 1322 A (Molecular Device, Sunnyvale, CA, USA). Recording pipette contained the following internal solution (in mM: 130 Cs-methanesulphonate, 10 CsCl, 4 NaCl, 1 $MgCl_2$, 10 HEPES, 5 EGTA, 2 QX-314, 12 phosphocreatine, 5 MgATP, 0.5 Na_2GTP, pH 7.2–7.3, 265–270 mOsm).

For spontaneous inhibitory postsynaptic current (sIPSC) recording, neurons were held at 0 mV, for excitatory postsynaptic current (sEPSC) recording, neurons were held at −70 mV. Evoked $GABA_A$R-IPSC (at 0 mV) and AMPAR-EPSC (at −70 mV) were generated with a series of pulses generated by S48 pulse stimulator (Grass Technologies, West Warwick, RI, USA) with different stimulation intensities (50–90 µA, 0.06 ms or 0.02 ms) delivered at 0.1 Hz. A bipolar stimulating electrode (FHC, Bowdoinham, ME) was placed ~100 µm from the neuron under recording. For paired-pulse ratios, $GABA_A$R-IPSC was evoked by double pulses with a 30 ms, 50 ms, or 100 ms interval, AMPAR-EPSC was evoked with 20 ms, 50 ms, or 100 ms interval.

To record the rheobase and evoked action potentials (eAP), slices were bathed in a modified ACSF with low (0.5 mM) $MgCl_2$ and high (3.5 mM) KCl, and recorded with the internal solution containing (in mM: 124 K-gluconate, 6 KCl, 1 $MgCl_2$, 5 EGTA, 10HEPES, 14 phosphocreatine, 5 Na_2ATP, 0.2 Na_2GTP, pH 7.2–7.3, 265–270 mOsm). A small depolarizing current was applied to adjust the membrane potential to −70 mV. For the recording of rheobase, a series of currents (starts from 0 pA, 5 pA increment, 1 s) were injected. For the recording of eAP, a series of currents (−20 to 160 pA, 60 pA increment, 1 s) were injected.

Co-immunoprecipitation (Co-IP)

As described in previous paper [7], transfected N2A cells were collected and homogenized with cold RIPA lysis buffer (mM: 150 NaCl, 50 Tris (pH = 8.0), 1% Nonidet P-40, 0.5% sodium deoxycholate, and 0.1% SDS) containing protease inhibitor. The lysates were incubated on ice for 30 min and then centrifuged at 12,000 g for 15 min at 4 °C. Supernatant fraction (40 µl) was collected as input control. The remainder was pre-cleared with Protein A/G plus agarose (Santa Cruz Biotechnology, sc-2003, 100 µl) for 1 hr at 4 °C. The pre-cleared supernatant was incubated overnight at 4 °C with antibodies against HDAC2 (Abcam, ab12169, 10 µg) or mouse IgG (sigma, 12–371, 10 µg) as negative control. Following incubation with 60 µl protein A/G plus agarose for 2 hr at 4 °C, immunoprecipitates were washed three times with lysis buffer and then boiled in 2× SDS loading buffer (40 µl). Western blotting was performed using antibodies against Smarcc2 (Cell Signaling, 12760, 1:1000), HDAC1 (Cell Signaling, 34589, 1:1000), and HDAC2 (Abcam, ab12169, 1:1000).

Chromatin immunoprecipitation (ChIP) assay

As previously described [9], GFP positive PFC from three mice were pooled per sample (50 mg in total). Each sample was homogenized in 250 µl ice cold douncing buffer with 1 ml 26-gauge syringe (15 strokes). Chromatin was digested using micrococcal nuclease (5 U/ml, Sigma, N5386) for 7 min at 37 °C, then the reaction was terminated by EDTA (10 mM, Invitrogen, 15575-038). Following lysis in 1 ml hypotonic lysis buffer (0.2 mM EDTA, pH 8.0, 0.1 mM benzamidine, 0.1 mM PMSF, 1.5 mM DTT) containing protease inhibitor on ice for 1 hr, lysates were centrifuged at 3000 g for 5 min at 4 °C. Supernatant (2–5%) was reserved as input control, while the remainder was pre-cleared with Salmon sperm DNA/protein A agarose-50% slurry (Millipore, 16–157) for 2 hr at 4 °C. Pre-cleared chromatin was incubated with antibodies against H3K9ac (10 µg per reaction; Sigma, 17-658) or Rabbit IgG (10 µg per reaction, Sigma, PP64B) overnight at 4 °C, followed by protein A agarose incubation for 2 hr. After washing, immunoprecipitates were eluted in 1% SDS and 0.1 M $NaHCO_3$. Crosslinks were reversed by incubation with 5 M NaCl (8 µl), 0.5 M EDTA (4 µl), 1 M Tris-HCl (pH 7.4, 8 µl), and 20 mg/ml proteinase K (0.4 µl, Thermo Fisher, EO0491) at 50 °C for 1 hr. DNA was purified

using the QIAquick PCR purification Kit (Qiagen, 28104) and eluted in 30 µl Buffer EB (Qiagen, 19086). ChIP-PCR was performed using primers targeting the promoter region of *Slc1a3* (Forward, 5′-GAGGACTGGGCTTGCATAGTT-3′; Reverse, 5′-TTCCTCCCATCCCA-GAGTCA-3′), *Slc6a1* (Forward, 5′-AGCCCTAGAGAGCTGAGAGGTT-3′; Reverse, 5′-GAGGACGGGGGACGATGC-3′), *Slc32a1* (Forward, 5′-CAAGAGCCAGACTGTCGTGA-3′; Reverse, 5′-ACTTGTTGGACACG-GAGGTG-3′). Quantification of ChIP signals was calculated as % input.

Statistical analysis

Statistical analysis was performed with GraphPad Prism 8.4.3. Data normality was assessed using the Shapiro-Wilk test before parametric analyses. Comparisons between two independent groups were conducted using two-tailed unpaired t-tests for normally distributed data, otherwise, the Mann-Whitney (M-W) test was applied. Comparisons of % change of mRNA levels were conducted with One Sample t test. For comparisons among more than two groups, one-way ANOVA was used for normally distributed data with homogeneity of variance, followed by Bonferroni *post hoc* tests for multiple comparisons, otherwise Kruskal-Wallis (K-W) test was performed, followed by pairwise Wilcoxon rank-sum tests with Bonferroni correction. In the social preference test, social versus nonsocial time was analyzed using two-way ANOVA. All data are presented as mean ± SEM. All experiments were replicated in multiple cohorts of animals and at least three independent in vitro experiments.

DATA AVAILABILITY

RNA-seq fastq files generated in this study are available at the Sequence Read Archive (Bioproject: PRJNA1449491). The count matrix for both mouse brain and hiPSC-N mRNA expression are deposited to the GEO public repository (GSE327210). Any additional data and code employed in this study can be made available upon request.

REFERENCES

1. Shenouda J, Barrett E, Davidow AL, Sidwell K, Lescott C, Halperin W, et al. Prevalence and disparities in the detection of autism without intellectual disability. Pediatrics. 2023;151:e2022056594.
2. Satterstrom FK, Kosmicki JA, Wang J, Breen MS, De Rubeis S, An JY, et al. Large-scale exome sequencing study implicates both developmental and functional changes in the neurobiology of autism. Cell. 2020;180:568–84.e523
3. Sanders SJ, Murtha MT, Gupta AR, Murdoch JD, Raubeson MJ, Willsey AJ, et al. De novo mutations revealed by whole-exome sequencing are strongly associated with autism. Nature. 2012;485:237–41.
4. Vissers LE, Gilissen C, Veltman JA. Genetic studies in intellectual disability and related disorders. Nat Rev Genet. 2016;17:9–18.
5. Yan Z. Targeting epigenetic enzymes for autism treatment. Trends Pharmacol Sci. 2024;45:764–7.
6. Qin L, Ma K, Wang ZJ, Hu Z, Matas E, Wei J, et al. Social deficits in Shank3-deficient mouse models of autism are rescued by histone deacetylase (HDAC) inhibition. Nat Neurosci. 2018;21:564–75.
7. Wang ZJ, Zhong P, Ma K, Seo JS, Yang F, Hu Z, et al. Amelioration of autism-like social deficits by targeting histone methyltransferases EHMT1/2 in Shank3-deficient mice. Mol Psychiatry. 2020;25:2517–33.
8. Katayama Y, Nishiyama M, Shoji H, Ohkawa Y, Kawamura A, Sato T, et al. CHD8 haploinsufficiency results in autistic-like phenotypes in mice. Nature. 2016;537:675–9.
9. Qin L, Williams JB, Tan T, Liu T, Cao Q, Ma K, et al. Deficiency of autism risk factor ASH1L in prefrontal cortex induces epigenetic aberrations and seizures. Nat Commun. 2021;12:6589.
10. Herrera ML, Paraíso-Luna J, Bustos-Martínez I, Barco Á. Targeting epigenetic dysregulation in autism spectrum disorders. Trends Mol Med. 2024;30:1028–46.
11. Lessard J, Wu JI, Ranish JA, Wan M, Winslow MM, Staahl BT, et al. An essential switch in subunit composition of a chromatin remodeling complex during neural development. Neuron. 2007;55:201–15.
12. He S, Wu Z, Tian Y, Yu Z, Yu J, Wang X, et al. Structure of nucleosome-bound human BAF complex. Science. 2020;367:875–81.
13. Fu JM, Satterstrom FK, Peng M, Brand H, Collins RL, Dong S, et al. Rare coding variation provides insight into the genetic architecture and phenotypic context of autism. Nat Genet. 2022;54:1320–31.
14. Barisic D, Stadler MB, Iurlaro M, Schübeler D. Mammalian ISWI and SWI/SNF selectively mediate binding of distinct transcription factors. Nature. 2019;569:136–40.
15. Clapier CR, Iwasa J, Cairns BR, Peterson CL. Mechanisms of action and regulation of ATP-dependent chromatin-remodelling complexes. Nat Rev Mol Cell Biol. 2017;18:407–22.
16. Machol K, Rousseau J, Ehresmann S, Garcia T, Nguyen TTM, Spillmann RC, et al. Expanding the spectrum of BAF-related disorders: de novo variants in SMARCC2 cause a syndrome with intellectual disability and developmental delay. Am J Hum Genet. 2019;104:164–78.
17. Bosch E, Popp B, Güse E, Skinner C, van der Sluijs PJ, Maystadt I, et al. Elucidating the clinical and molecular spectrum of SMARCC2-associated NDD in a cohort of 65 affected individuals. Genet Med. 2023;25:100950.
18. Narayanan R, Pirouz M, Kerimoglu C, Pham L, Wagener RJ, Kiszka KA, et al. Loss of BAF (mSWI/SNF) complexes causes global transcriptional and chromatin state changes in forebrain development. Cell Rep. 2015;13:1842–54.
19. Tuoc T, Dere E, Radyushkin K, Pham L, Nguyen H, Tonchev AB, et al. Ablation of BAF170 in developing and postnatal dentate gyrus affects neural stem cell proliferation, differentiation, and learning. Mol Neurobiol. 2017;54:4618–35.
20. Tuoc TC, Boretius S, Sansom SN, Pitulescu ME, Frahm J, Livesey FJ, et al. Chromatin regulation by BAF170 controls cerebral cortical size and thickness. Dev Cell. 2013;25:256–69.
21. Reinert S, Hübener M, Bonhoeffer T, Goltstein PM. Mouse prefrontal cortex represents learned rules for categorization. Nature. 2021;593:411–7.
22. Yan Z, Rein B. Mechanisms of synaptic transmission dysregulation in the prefrontal cortex: pathophysiological implications. Mol Psychiatry. 2022;27:445–65.
23. Stoner R, Chow ML, Boyle MP, Sunkin SM, Mouton PR, Roy S, et al. Patches of disorganization in the neocortex of children with autism. N Engl J Med. 2014;370:1209–19.
24. d'Isa R, Comi G, Leocani L. Apparatus design and behavioural testing protocol for the evaluation of spatial working memory in mice through the spontaneous alternation T-maze. Sci Rep. 2021;11:21177.
25. Conrow-Graham M, Williams JB, Martin J, Zhong P, Cao Q, Rein B, et al. A convergent mechanism of high risk factors ADNP and POGZ in neurodevelopmental disorders. Brain. 2022;145:3250–63.
26. Rein B, Ma K, Yan Z. A standardized social preference protocol for measuring social deficits in mouse models of autism. Nat Protoc. 2020;15:3464–77.
27. Li P, Yan Z. An epigenetic mechanism of social isolation stress in adolescent female mice. Neurobiol Stress. 2024;29:100601.
28. Hyun K, Ahn J, Kim H, Kim J, Kim Y-I, Park H-S, et al. The BAF complex enhances transcription through interaction with H3K56ac in the histone globular domain. Nat Commun. 2024;15:9614.
29. Douglas RJ, Martin KA. Neuronal circuits of the neocortex. Annu Rev Neurosci. 2004;27:419–51.
30. Morishima M, Morita K, Kubota Y, Kawaguchi Y. Highly differentiated projection-specific cortical subnetworks. J Neurosci. 2011;31:10380–91.
31. Hernandez Carballo LG, Li P, Senek R, Yan Z. Systemic histone deacetylase inhibition ameliorates the aberrant responses to acute stress in socially isolated male mice. J Physiol. 2024;602:2047–60.
32. Brahma S, Henikoff S. The BAF chromatin remodeler synergizes with RNA polymerase II and transcription factors to evict nucleosomes. Nat Genet. 2024;56:100–11.
33. Mashtalir N, D'Avino AR, Michel BC, Luo J, Pan J, Otto JE, et al. Modular organization and assembly of SWI/SNF family chromatin remodeling complexes. Cell. 2018;175:1272–88.e1220
34. Wilson BG, Roberts CW. SWI/SNF nucleosome remodellers and cancer. Nat Rev Cancer. 2011;11:481–92.
35. Kadoch C, Crabtree GR. Mammalian SWI/SNF chromatin remodeling complexes and cancer: mechanistic insights gained from human genomics. Sci Adv. 2015;1:e1500447.
36. Valencia AM, Sankar A, van der Sluijs PJ, Satterstrom FK, Fu J, Talkowski ME, et al. Landscape of mSWI/SNF chromatin remodeling complex perturbations in neurodevelopmental disorders. Nat Genet. 2023;55:1400–12.
37. Habib A, Harris L, Pollick F, Melville C. A meta-analysis of working memory in individuals with autism spectrum disorders. PLoS One. 2019;14:e0216198.
38. Gangopadhyay P, Chawla M, Dal Monte O, Chang SWC. Prefrontal-amygdala circuits in social decision-making. Nat Neurosci. 2021;24:5–18.
39. Park G, Ryu C, Kim S, Jeong SJ, Koo JW, Lee YS, et al. Social isolation impairs the prefrontal-nucleus accumbens circuit subserving social recognition in mice. Cell Rep. 2021;35:109104.

40. Qi C, Sima W, Mao H, Hu E, Ge J, Deng M, et al. Anterior cingulate cortex parvalbumin and somatostatin interneurons shape social behavior in male mice. Nat Commun. 2025;16:4156.
41. Liu D, Rahman M, Johnson A, Amo R, Tsutsui-Kimura I, Sullivan ZA, et al. A hypothalamic circuit underlying the dynamic control of social homeostasis. Nature. 2025;640:1000–10.
42. Packard K, Opendak M. Rodent models of early adversity: impacts on developing social behavior circuitry and clinical implications. Front Behav Neurosci. 2022;16:918862.
43. Bourgeron T. From the genetic architecture to synaptic plasticity in autism spectrum disorder. Nat Rev Neurosci. 2015;16:551–63.
44. Cho H, Yoo T, Moon H, Kang H, Yang Y, Kang M, et al. Adnp-mutant mice with cognitive inflexibility, CaMKIIα hyperactivity, and synaptic plasticity deficits. Mol Psychiatry. 2023;28:3548–62.
45. Jung EM, Moffat JJ, Liu J, Dravid SM, Gurumurthy CB, Kim WY. Arid1b haploinsufficiency disrupts cortical interneuron development and mouse behavior. Nat Neurosci. 2017;20:1694–707.
46. Wamsley B, Bicks L, Cheng Y, Kawaguchi R, Quintero D, Margolis M, et al. Molecular cascades and cell type-specific signatures in ASD revealed by single-cell genomics. Science. 2024;384:eadh2602.
47. Qiao Y, Wang R, Yang X, Tang K, Jing N. Dual roles of histone H3 lysine 9 acetylation in human embryonic stem cell pluripotency and neural differentiation. J Biol Chem. 2015;290:2508–20.
48. Creyghton MP, Cheng AW, Welstead GG, Kooistra T, Carey BW, Steine EJ, et al. Histone H3K27ac separates active from poised enhancers and predicts developmental state. Proc Natl Acad Sci USA. 2010;107:21931–6.
49. Cai Y, Zhang Y, Loh YP, Tng JQ, Lim MC, Cao Z, et al. H3K27me3-rich genomic regions can function as silencers to repress gene expression via chromatin interactions. Nat Commun. 2021;12:719.
50. Tseng CJ, McDougle CJ, Hooker JM, Zürcher NR. Epigenetics of autism spectrum disorder: histone deacetylases. Biol Psychiatry. 2022;91:922–33.
51. Ramaswami G, Won H, Gandal MJ, Haney J, Wang JC, Wong CCY, et al. Integrative genomics identifies a convergent molecular subtype that links epigenomic with transcriptomic differences in autism. Nat Commun. 2020;11:4873.
52. Rein B, Conrow-Graham M, Frazier A, Cao Q, Yan Z. Inhibition of histone deacetylase 5 ameliorates abnormalities in 16p11.2 duplication mouse model. Neuropharmacology. 2022;204:108893.
53. Sun W, Poschmann J, Cruz-Herrera Del Rosario R, Parikshak NN, Hajan HS, Kumar V, et al. Histone acetylome-wide association study of autism spectrum disorder. Cell. 2016;167:1385–97.e1311
54. Wang W, Tan T, Cao Q, Zhang F, Rein B, Duan WM, et al. Histone deacetylase inhibition restores behavioral and synaptic function in a mouse model of 16p11.2 deletion. Int J Neuropsychopharmacol. 2022;25:877–89.
55. Gandal MJ, Haney JR, Wamsley B, Yap CX, Parhami S, Emani PS, et al. Broad transcriptomic dysregulation occurs across the cerebral cortex in ASD. Nature. 2022;611:532–9.
56. Bachmann C, Nguyen H, Rosenbusch J, Pham L, Rabe T, Patwa M, et al. mSWI/SNF (BAF) complexes are indispensable for the neurogenesis and development of embryonic olfactory epithelium. PLOS Genet. 2016;12:e1006274.
57. Yang G, Ren Y, Zhong P, Patel PJ, Chen XQ, Wan L, et al. Histone demethylase PHF2 regulates inflammatory genes in Alzheimer's disease. Mol Psychiatry. 2026;31:845–59.
58. Deacon RMJ, Rawlins JNP. T-maze alternation in the rodent. Nat Protoc. 2006;1:7–12.
59. Lin CH, Yu M, Patel PJ, Li P, Yan Z. Epigenetic treatment of synaptic and behavioral deficits in Dyrk1a-mutant mice. Neuropsychopharmacology. 2026;51:1413–23.
60. Kulesskaya N, Voikar V. Assessment of mouse anxiety-like behavior in the light-dark box and open-field arena: role of equipment and procedure. Physiol Behav. 2014;133:30–38.
61. Jiang H, Xiao Z, Saleem K, Zhong P, Li L, Chhetri G, et al. Generation of human induced pluripotent stem cell-derived cortical neurons expressing the six tau isoforms. J Alzheimers Dis. 2025;105:1341–54.
62. Saleem K, Xiao Z, Zhu B, Ren Y, Yan Z, Feng J. Elevated SGK1 increases Tau phosphorylation and microtubule instability in Alzheimer's patient-derived cortical neurons. Mol Psychiatry. 2026;31:332–42.
63. Xie Z, Bailey A, Kuleshov MV, Clarke DJB, Evangelista JE, Jenkins SL, et al. Gene set knowledge discovery with enrichr. Curr Protoc. 2021;1:e90.
64. Heberle H, Meirelles GV, da Silva FR, Telles GP, Minghim R. InteractiVenn: a web-based tool for the analysis of sets through Venn diagrams. BMC Bioinforma. 2015;16:169.
65. Szklarczyk D, Gable AL, Nastou KC, Lyon D, Kirsch R, Pyysalo S, et al. The STRING database in 2021: customizable protein-protein networks, and functional characterization of user-uploaded gene/measurement sets. Nucleic Acids Res. 2021;49:D605–d612.
66. Tan T, Wang W, Williams J, Ma K, Cao Q, Yan Z. Stress exposure in dopamine D4 receptor knockout mice induces schizophrenia-like behaviors via disruption of GABAergic transmission. Schizophr Bull. 2019;45:1012–23.

ACKNOWLEDGEMENTS

We thank Xiaoqing Chen for her excellent technical support.

AUTHOR CONTRIBUTIONS

PL performed animal surgery, immunostaining, behavioral, qPCR, and biochemical experiments, and wrote the draft. SM performed animal surgery and electrophysiological experiments. PJP and ZY performed bioinformatics analysis. PZ performed earlier electrophysiological experiments. KS, KWT and JF performed experiments with hiPSC-derived neurons. ZY supervised the project and edited the paper.

FUNDING

This work was supported by a grant from the National Institutes of Health NS127728 to Z.Y. and J.F.

COMPETING INTERESTS

The authors declare no competing interests.

ADDITIONAL INFORMATION

Supplementary information The online version contains supplementary material available at https://doi.org/10.1038/s41380-026-03848-1.

Correspondence and requests for materials should be addressed to Zhen Yan.

Reprints and permission information is available at http://www.nature.com/reprints

Publisher's note Springer Nature remains neutral with regard to jurisdictional claims in published maps and institutional affiliations.